Aeroelastic Stability of Idling Wind Turbines

Kai Wang[1], Vasilis A. Riziotis[2], Spyros G. Voutsinas[2]

[1] China-EU Institute for Clean and Renewable Energy, Huazhong University of Science and Technology, 1037 Luoyu Rd, Wuhan, China

[2] School of Mechanical Engineering, National Technical University of Athens, GR15780 Athens, Greece

Correspondence to: Vasilis A. Riziotis (vasilis@fluid.mech.ntua.gr)

Abstract. Wind turbine rotors in idling operation mode can experience high angles of attack, within the post stall region that are capable of triggering stall-induced vibrations. The aim of the present paper is to extend existing knowledge on dynamics and aerodynamics of an idling wind turbine and characterize its stability. Rotor stability in slow idling operation is assessed on the basis of nonlinear time domain and linear eigenvalue analyses. The aim is to check when linear analysis is reliable and identify cases for which non-linear effects are significant. Analysis is performed for a 10 MW conceptual wind turbine designed by DTU. First, the flow conditions that are likely to favour stall induced instabilities are identified through nonlinear time domain aeroelastic simulations. Next, for the above specified conditions, eigenvalue stability analysis is performed aiming at identifying the low damped modes of the turbine. The eigenvalue stability results are evaluated through computations of the work of the aerodynamic forces under imposed harmonic motion following the shape and frequency of the various modes. Nonlinear work characteristics predicted by ONERA and Beddoes-Leishman dynamic stall models are compared. Both eigenvalue and work analyses indicate that the asymmetric and symmetric out-of-plane modes have the lowest damping. The results of the eigenvalue analysis agree well with those of the nonlinear work analysis and the time domain simulations.

1   Introduction

In idling mode, the angles of attack (AOA) experienced by the blades significantly vary over one revolution under the combined effect of inflow turbulence, flow inclination and nacelle tilt and yaw. The variation of the AOAs remains substantial even in small yaw misalignments within the range of +/-15°. It is noted that yaw errors in this range are considered as normal idling conditions by wind turbine manufactures. Going to moderate yaw angles, the variations of the AOA can be such that the rotor enters stall both at positive and negative AOAs and thereby stall induced vibrations are likely to occur. In the past, a lot of research effort has been directed to the analysis of stall induced vibrations (SIV) in normal operation, (Petersen et al, 1998; Hansen, 2003; Riziotis et al, 2004; Hansen, 2007), however very little has been done for parked or idling rotors.

Aeroelastic analysis of parked or idling rotors mostly relies on blade element aerodynamic models. BEM models comply with industry's needs for fast aerodynamic tools, capable of performing certification simulations. In the context of blade element models, Politis et al (2009) investigated the stability characteristics of an isolated parked blade at various inflow

angles using an eigenvalue approach and considering steady-state but also unsteady aerodynamics. That paper focused on stall induced instabilities. It was shown that such instabilities can take place at inflow angles that slightly exceed C_{Lmax} AOA but also in the vicinity of +/-90° AOA. In a similar context Skrzypiński & Gaunaa (2015) investigated the stability of an elastically mounted 2D section of the parked blade using engineering aerodynamic models. In their work, they investigated the effect of imposing temporal lag on the steady-state aerodynamic loads at very high AOA by using indicial functions. Despite the fact that the choice of the lag response was not based on measured information - a rather intuitive tuning of the model parameters has been performed -it was shown that in all cases an increase in the damping of the low damped edgewise modes is finally obtained even for very small delay values. In their work the authors have also investigated the effect of various structural parameters on the damping characteristics of a parked blade. Very recently Pirrung et al (2016) proposed a new hybrid model for the analysis of parked/idling rotors. The model is based on the coupling of a trailed vortex near wake model with a momentum type far wake model. In their work the authors have only presented time domain aerodynamic analysis results. However, the formulated model is linearizable and therefore can serve for eigenvalue aeroelastic stability analyses.

Although CFD models are still computationally expensive, especially in view of performing extensive time domain certification simulations, some work has been done at the level of advanced aerodynamic models. Skrzypiński et al (2014a) investigated stall induced vibrations using 2D RANS and 3D DES aerodynamic simulations for a typical elastically mounted blade section in combined flap-edge motion. The 3D simulations considered an extruded section and periodic spanwise flow conditions. The analysis focused on AOA that slightly exceed C_{Lmax}. It was concluded that the differences in the predicted post stall characteristics and the stability limits between 2D and 3D CFD analysis are significant. Skrzypiński et al (2014b) also investigated vortex shedding phenomena occurring at very high AOA, in the vicinity of 90° using CFD models. Also in this work, a typical elastically mounted blade section was considered. AOA of about 90° can be encountered by a wind turbine blade during the installation phase or in case of a yaw system failure. Under such flow conditions vortex shedding phenomena can be combined with negative slopes of the lift curve that favour combined stall and vortex induced vibrations (VIV). Typical section analysis showed that lock-on at the vortex shedding frequency is likely to occur depending on the amplitude of the lead-lag motion undergone by the section. Finally, Heinz et al (2016) analysed the full blade configuration at 90° AOA using a DES aerodynamic model coupled to a nonlinear beam model of the blade. The analyses showed that at certain azimuth positions of the parked blade when the inflow has a significant velocity component along the blade axis, spanwise correlated vortex shedding over large parts of the blade can be triggered which eventually leads to excessive VIV.

Vortex shedding phenomena and VIV have been also investigated by Zou et al (2014) with vortex modeling. Massive flow separation over the blade surface was simulated in the context of the "double wake" concept. The "double wake" concept is based on the modeling principle that the flow separation bubble can be simulated by two vortex sheets one originating from the trailing edge of the blade and the other from the position where separation of the flow takes place. The work focused on a typical, elastically mounted blade section at high AOA and showed that VIV and lock-on phenomena are likely to occur at lower wind speeds while at higher wind speeds edgewise instabilities are mainly driven by the negative

slope of the lift curve at AOA in the vicinity of 90°. An important result of this work which confirms the findings of Skrzypiński & Gaunaa (2015), is that the unsteady character of the flow (temporal lag) increases the damping of the low damped edgewise modes at very high AOA and by that indicates that steady-state analysis is expected to be conservative.

In the present paper the stability behaviour of the conceptual 10 MW reference wind turbine (3 bladed, pitch regulated-variable speed turbine with diameter D=178.3 m) designed by DTU Wind Energy (Bak et al, 2013) in slow idling operation is assessed using the linear eigenvalue stability tool GAST_lin (Riziotis et al, 2004). The objectives of the work are to first identify idling situations at moderate yaw misalignment angles, that favour stall induced vibrations and subsequently predict which of the turbine modes exhibit the lowest damping characteristics. The analysis is confined to yaw angles within the range [-60°, +60°]. This is the absolute upper limit up to which engineering dynamic stall models can be trusted. Outside this range deep stall conditions are encountered that cannot be properly addressed by engineering aerodynamic models. This is because engineering models lack the appropriate tuning in such deep stall conditions. Furthermore, in deep stall, vortex shedding phenomena take place that lead to additional periodic excitation of the rotor not included in the present engineering modeling framework.

The eigenvalue analysis results are compared against results of nonlinear time domain analysis as well as with results of aerodynamic work computations coming from forced harmonic oscillation simulations in which the imposed motion follows the shape and the frequency of the turbine modes. This is done in an attempt to prove that fast linear eigenvalue stability tools that have been widely employed by the industry for damping characterization in normal operation conditions can be also trusted for predicting damping in idling operation conditions.

The inflow conditions that favour stall induced instabilities are identified through turbulent wind nonlinear time domain aeroelastic simulations at yaw angles in the range [-60°, +60°] (moderate to high yaw angles) using the hGAST aeroelastic modeling platform (Manolas et al, 2015). As already mentioned the above range of yaw angles defines the validated envelope of engineering dynamic stall models. Rotor azimuth positions and corresponding sectional AOAs at which instabilities are favoured are assessed. Moreover, the average rotor speeds for the different yaw angles are recorded in order to be used as input to the linear eigenvalue stability tool.

Based on the findings of the above time domain analysis, eigenvalue stability analysis is performed focusing on the conditions for which maximum edgewise loads are obtained with hGAST code. Stability analysis in the case of yaw misalignment requires application of Floquet's theory (Skjoldan & Hansen, 2009; Bottasso & Cacciola, 2015). This is because in yawed flows, periodicity on aerodynamic loads, introduced as a result of non axi-symmetric inflow conditions, cannot be eliminated through application of Coleman's multi-blade transformation. Besides the anyway high cost of Floquet analysis, in idling conditions the rotational speed attains very low values that become at least ten times smaller than the lowest natural frequency of the turbine which further increases the cost to a prohibitive level for the here intended analysis. As an alternative, standard eigenvalue analysis could be instead performed on the Coleman transformed system for some "averaged" over one revolution coefficients. However, if this could be done, it would be only in cases of "moderate" periodicity. To the authors opinion extending this approach to cases of 30 deg or even 60 deg yaw angles would be definitely

questionable. On the other hand, by noting that at very small rotational speeds (~1 RPM) low order harmonics (up to 6p) are not expected to interact strongly with the natural frequencies of the turbine, as a second alternative, non-rotating (static) analysis can be performed at different azimuth angles within the sector [0°, 120°]. The latter approach is followed in the present work. In order to approximate as closely as possible, the rotating case a free-free drive train (free rotation boundary condition over the generator side) is simulated and the idling rotational speed (obtained through time domain simulations) is taken into account in formulating the local to the blade section velocity triangle.

Finally, using as input the aeroelastic mode shapes and frequencies calculated through the eigenvalue analysis, aerodynamic work computations are performed. The turbine is set to a prescribed small amplitude harmonic motion following the shape and frequency of the various aeroelastic modes. The work done by the aerodynamic loads acting on the blades as a result of this forced vibration, is computed over one oscillation cycle. This work is directly related to the damping of the corresponding mode (Petersen et al, 1998). Nonlinear work computations are compared to eigenvalue analysis results.

The present work is a follow up of the work presented in Wang et al (2016). The dynamic stall model used in calculating the aerodynamic loads in deep stall is critical for the assessment of the stability limits of an idling turbine. The innovative contribution of the present work in relation to the previous work presented in Wang et al (2016) is that in the present work emphasis is put in describing in detail the ONERA model employed in hGAST aeroelastic code for the prediction of the aerodynamic loads in dynamic stall (Sect. 3.2). Moreover, validation of the model in deep stall conditions is presented in the same section. Predictions of the ONERA model are compared to measured data for pitching airfoils in deep stall, well beyond the C_{Lmax} AOA, and to results of the state-of-the-art Beddoes Leishman model. Finally, work computations are performed in Sect. 4.3 using both unsteady aerodynamic models as well as steady state aerodynamics. In this way, the range of anticipated damping predictions in idling operation is better explored.

The results of the analysis indicated that the asymmetric and symmetric out-of-plane modes exhibit the lowest damping values. Among them, the asymmetric edge horizontal/tilt mode obtains negative damping values at the yaw angle of 30°. The results of the eigenvalue analysis agree well with the results of the time domain analysis.

2 Background on the dynamics and aerodynamic loading of an idling turbine

In the present section some important features related to the dynamics and aerodynamics of an idling turbine are discussed. This background information is regarded essential to render stability results presented in the following sections intelligible.

2.1 Modal characteristics of the idling turbine

Figure 1 presents the variation of the natural frequencies of the idling Reference 10 MW wind turbine versus pitch angle (calculated by hGAST aeroelastic code) as it increases from 0° to 90° (towards feather). This plot is typically very similar for any three bladed turbine of similar design philosophy. As expected, the two first tower modes M1 and M2 are not affected at all by the change in the pitch angle. The frequencies of the first asymmetric flap modes M3 and M4 slightly increase while the frequencies of the first asymmetric edgewise modes M6 and M7 significantly decrease as the pitch angle increases. As a

result, asymmetric flapwise and edgewise modes come closer in frequency to each other, despite their initial distinct separation at 0° pitch angle. Bringing the asymmetric flap and edge modes closer will render the cross coupling between the corresponding bending directions stronger when the blades are in feather position. The frequency of the first symmetric out of plane mode M5 will gradually increase and finally at high pitch angles will exceed the frequency of the asymmetric edgewise modes M6 and M7. The frequency of the first symmetric in-plane (drive train) mode M8 decreases with the pitch angle and as the pitch tends to 90° the frequency of M8 tends to coincide with the frequency of the symmetric out of plane mode M5. The second asymmetric flapwise modes M9 and M10 exhibit a similar behaviour with the first asymmetric flapwise modes M3 and M4.
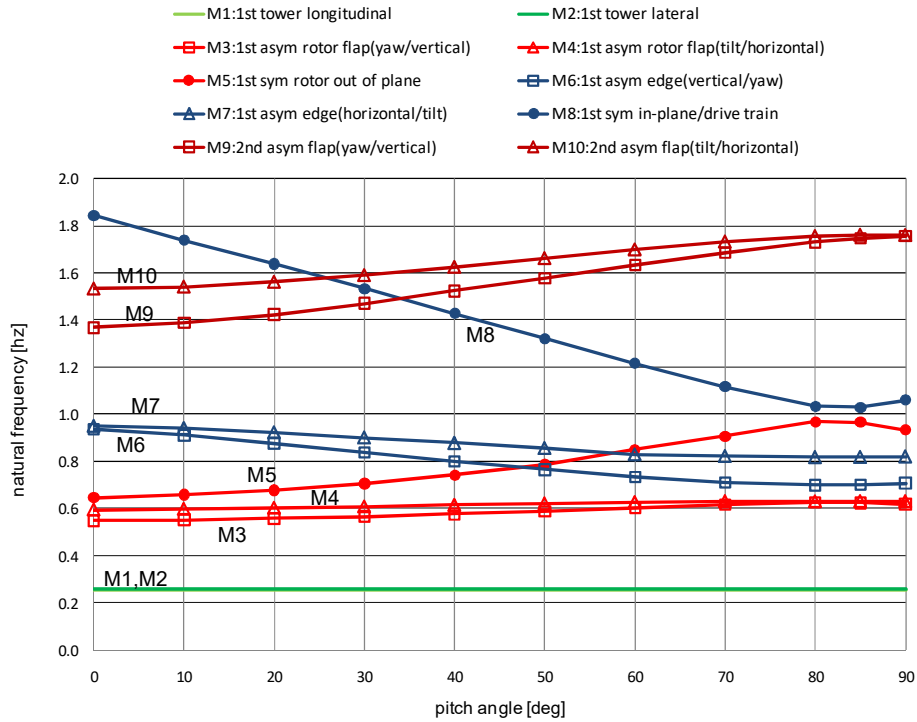
Figure 1. Natural frequencies of the 10 MW Reference Wind Turbine vs. pitch from 0° to 90° (towards feather).

As the blade pitches to feather, the asymmetric flapwise modes switch from out-of-plane to in-plane. Inversely the asymmetric edgewise modes switch from in-plane to out-of-plane. So, as the blade pitch changes from 0° to 90° the first asymmetric edgewise (in-plane) vertical mode M6 turns into a first asymmetric edgewise (out-of-pane) yawing mode and the first asymmetric edgewise (in-plane) horizontal mode M7 turns into a first asymmetric edgewise (out-of-pane) tilting mode. This transformation of the asymmetric edgewise modes is depicted in Figure 2(a) and (b). Inversely the first asymmetric flapwise (out-of-plane) yawing mode M3 turns into a first asymmetric flapwise (in-plane) vertical mode and the first

asymmetric flapwise (out-of-plane) tilting mode M4 turns into a first asymmetric flapwise (in-plane) horizontal mode. Similar transformations are obtained in the second flapwise modes M9 and M10.

On the other hand the symmetric modes seem to retain their original character. So, as shown in Figure 3 the out-of-plane (flapwise) collective mode (M5) remains a collective out-of-plane (edgewise) mode as the pitch changes from 0° to 90°. At 0° pitch the coupling with the in-plane direction in M5 is negligible. At 90°, as the frequency of M5 gets close to the frequency of the collective in-plane M8 mode a coupling with the in-plane direction is established.

(a)   (b)
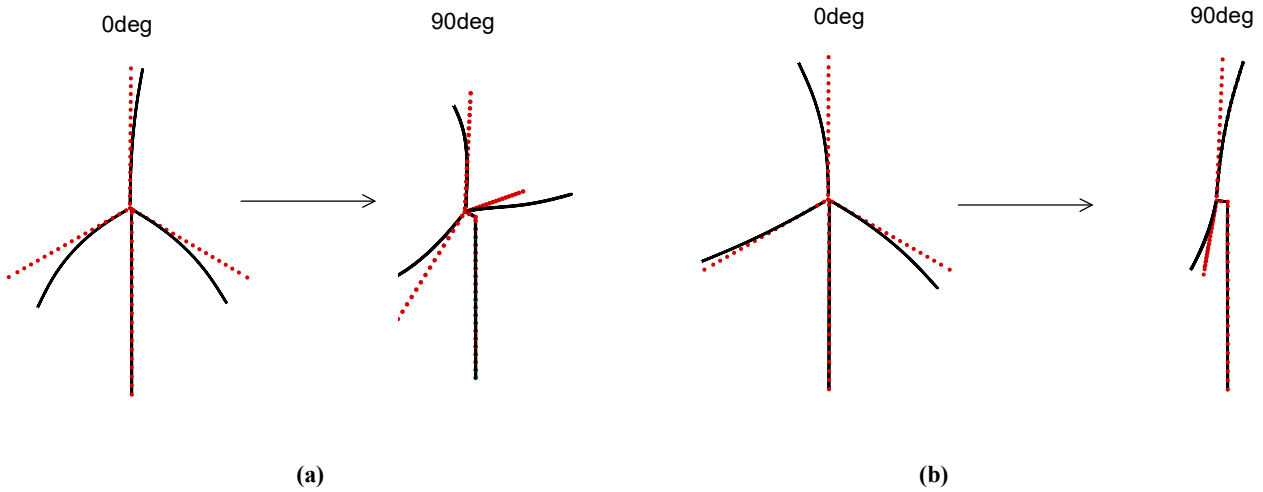
Figure 2. Mode shape alternation from 0° to 90° pitch for asymmetric edgewise modes (a) M6 and (b) M7. Red symbols: undeformed state, Black lines: deformed state.
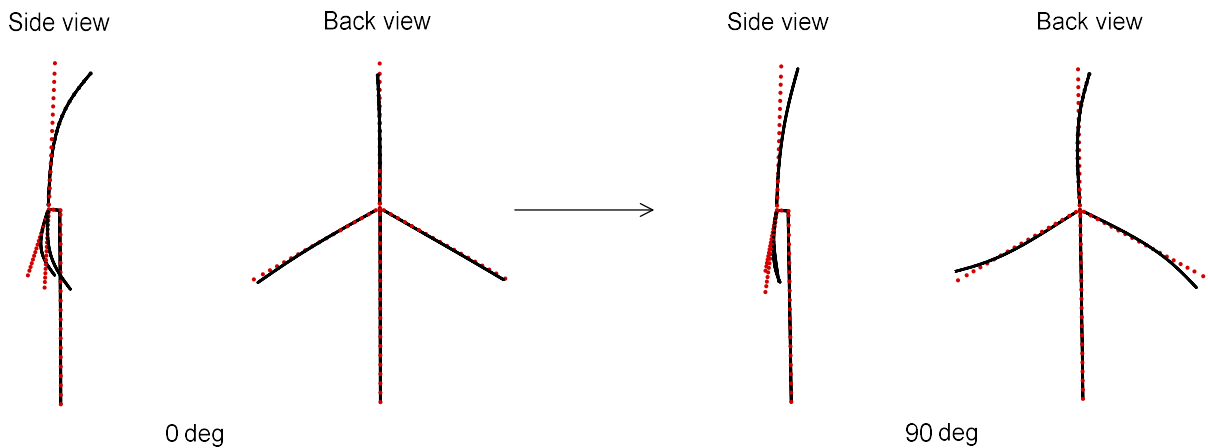
Figure 3.Mode shape alternation from 0° to 90° pitch for symmetric out-of-plane mode M5. Red symbols: undeformed state, Black lines: deformed state.

Also, as shown in Figure 4 the in-plane (edgewise) collective mode M8 remains a collective in-plane (flapwise) mode as the pitch changes from 0° to 90°. Originally, at 0° pitch a coupling with the second flapwise modes is clearly noted in the

shape of the mode, driven by the fact that the collective in-plane mode lies closely to the second flapwise asymmetric modes. At 90° pitch, as the frequency of the mode decreases and approaches the frequency of the first collective out-of-plane mode a coupling with this mode is activated.
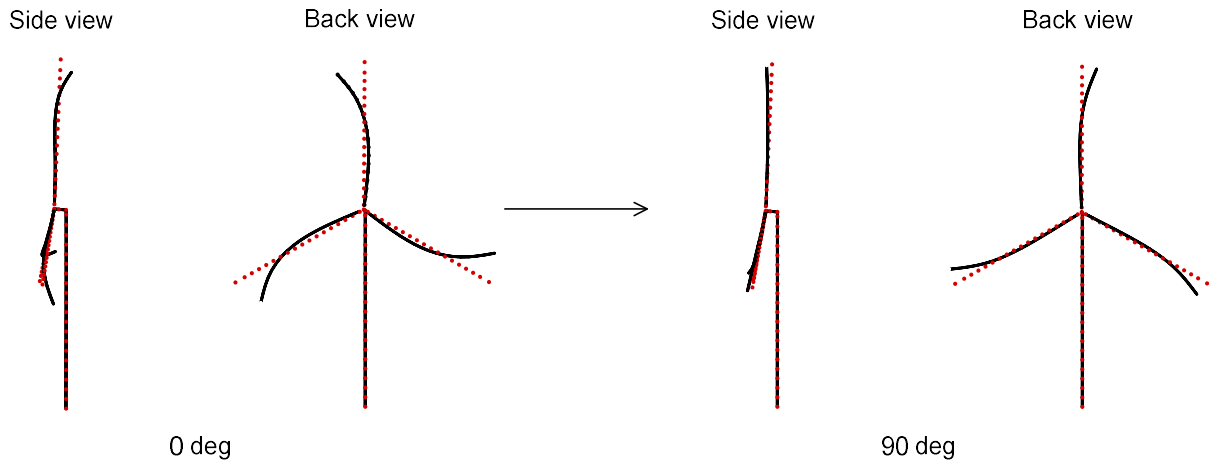
Figure 4.Mode shape alternation from 0° to 90° pitch for symmetric in-plane mode M8. Red symbols: undeformed state, Black lines: deformed state.

2.2 Aerodynamic characteristics of the idling rotor

As already discussed the AOAs experienced by the blades of an idling rotor vary significantly over the revolution. The velocity triangle of a section of an idling blade is illustrated in Figure 5 for the blade azimuth positions of 0°, 90°, 180° and 270°. It is seen that as a result of yaw error the AOA reaches a minimum/ maximum at 0°/180° azimuth respectively (whether the AOA will be positive or negative depends on the direction of the incoming flow – positive or negative yaw) while as a result of tilt and inflow inclination angles the AOA attains a minimum at 90° and a maximum at 270°. An example of the AOA variation of the 75% section of the reference 10 MW is shown in Figure 6 (a) for a yaw angle of 15° and a tilt angle of 5°. The mean wind speed and the pitch setting are taken equal to 42.5 ms^{-1} and 90° respectively; the blade section is considered to have zero twist and the linear speed component due to the idling rotation of the blade is not taken into account (assuming an almost zero idling speed). It is seen that as the yaw angle increases the range of variation of the AOA equally increases. The range of variation of the AOA is equal to the yaw error angle. Moreover, superposition of inflow turbulence further increases the range of AOA variation. If the yaw error is combined with the tilt of the rotor (or the inclination of the mean inflow) then the range of variation of the AOA increases further. The azimuth angle for which maximum (positive or negative) AOA is obtained is shifted away from 0° and 180° given the 90° phase difference of the two effects. Beyond a certain yaw angle the blade will definitely enter stall both in the positive and the negative AOAs regime.

As the pitch of the blade increases towards feather the local AOAs "seen" by the blade are equally shifted to lower values and therefore idling speed decreases. On the other hand, reduction of the idling speed leads to higher AOAs along the blade

span. An example of the effect of the idling speed on the AOAs of the 75% section is shown in Figure 6(b). For an inflow velocity of 42.5 ms^{-1} an almost 10° increase of the AOAs is noted as the idling speed decreases from 1 RPM to almost 0 RPM. So, the pitch angle of the blade and the rotor idling speed are two interrelated but also competing parameters as concerns the mean level of the AOA variation.
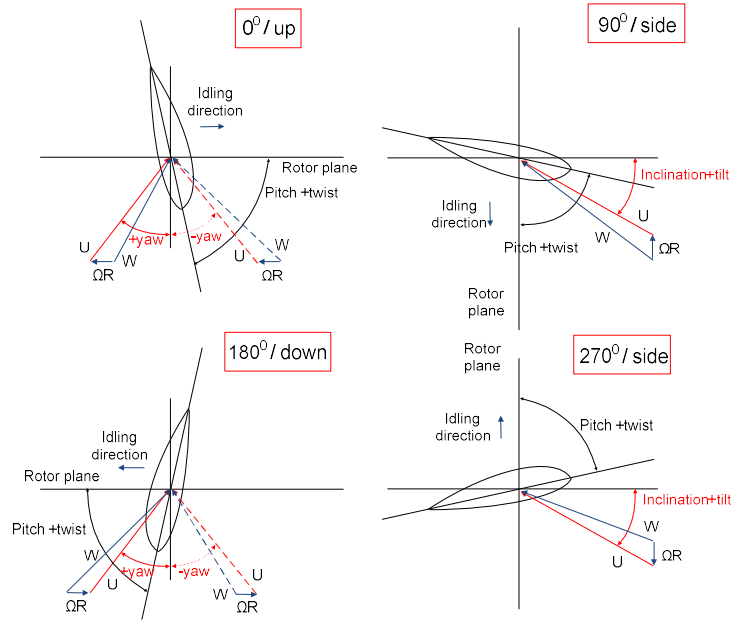
Figure 5. Velocity triangles of idling blade at different azimuth positions.

(a)   (b)
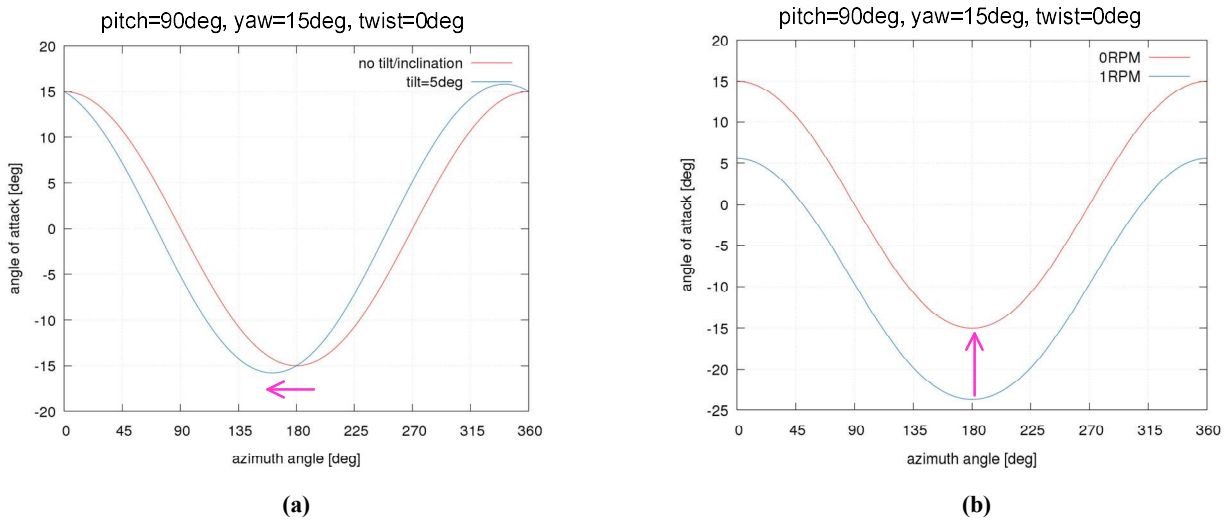
Figure 6. Variation of the angle of attack over one revolution for a wind speed of 42.5 ms^{-1} (a) effect of yaw and tilt angle - tilt angle shifts the curve horizontally, the rotational speed is almost zero), (b) effect of rotational speed - the rotational speed shifts the curve vertically.

Whether stall induced vibrations will appear on an idling rotor, depends strongly on the post stall characteristics of the airfoil sections forming the blade. Higher negative slopes of the C_L curve and deeper drop of the C_L in the post stall region deteriorates stability characteristics. As already mentioned for moderate to high yaw angles the idling blade enters stall both at positive and negative AOAs. The post stall characteristics of cambered sections differ significantly between positive and negative AOA. Usually, airfoil sections exhibit smoother post stall behaviour at negative AOAs compared to that at positive ones (there are of course exceptions to the above statement). This implies that selection of the appropriate pitch setting and thereby of the appropriate idling speed could be critical in several cases when targeting the avoidance of stall induced vibrations. Adjustment of the blade pitch may shift the AOAs to a favourable range.

3   Description of tools

3.1 Description of the aeroelastic tool

Nonlinear time domain aeroelastic simulations are performed using NTUA's in-house servo-aero-elastic solver hGAST (Manolas et al, 2015). Stability analysis is performed using the eigenvalue stability tool GAST_lin (Riziotis et al, 2004) which is a linearized version of the nonlinear hGAST code. In both hGAST and GAST_lin solvers, the full wind turbine is considered as a multi-component dynamic system having as components the blades, the drive train and the tower; all approximated as Euler-Bernoulli or Timoshenko beam structures. Assembly of the above components into the full system is carried out in the framework of the so called multibody approach. It consists of considering each component separately from the others but subjected to specific free-body kinematic and loading conditions that are imposed at the connection points of the components.

In the multibody context, a local coordinate system (see Figure 7(a)) is assigned to each component/body with respect to which local elastic displacements are defined. In GAST_lin the local frame of each body is subjected to rigid body and elastic motions communicated by preceding bodies as kinematic conditions imposed at their connection points. Rigid body motions can be either prescribed or controlled while elastic motions consist of the total deflection of the previous components "transferred" to the current component. For example, the blades are subjected to elastic translational and rotational motions of the drive train and the tower(see Figure 7(b))as well as to rigid body motions asthe pitch motion and teetering motion of two bladed rotors (directly imposed to the blades - see Figure 7(c)), azimuthal rotation, yaw rotation (indirectly imposed to the blades through the drive train and the nacelle - see Figure 7(c)), foundation motions or motions of the supporting structure in case of floating wind turbines(indirectly imposed to the blades through the tower - see Figure 7(c)). In addition to the kinematic conditions imposed at the connection points, loading conditions must be also satisfied. In particular, at each connection point, one of the connected bodies contributes the displacements and rotations to all others, which in turn contribute their internal (reaction) loads.

The advantage of the above formulation in comparison to other multi-body formulations applying the Lagrange multipliers approach is that the resulting dynamic equations of motion can be easily linearized analytically and thereafter linear eigenvalue stability analysis can be performed with respect to a highly deflected steady or periodic state.

| (a) | (b) | (c) |
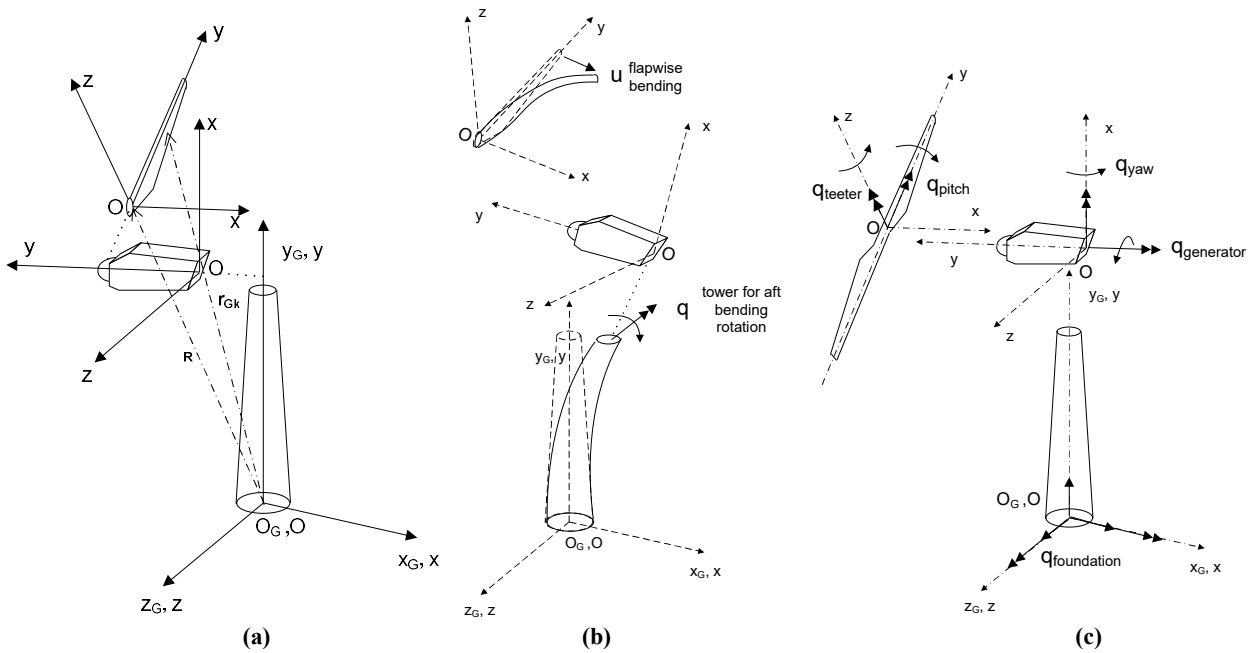
Figure 7. (a)Wind turbine inertial frame and local frame of the various components, (b) Realization of multibody kinematics, examples of elastic q DOFs ,(c) Realization of multibody kinematics, examples of controlled or free motion q DOFs.

The same multi-body formulation is also extendable to the component level which is actually implemented in hGAST.
Highly flexible components, such as the blades, are divided into a number of interconnected sub-bodies, each considered as a
10 single linear beam element or as an assembly of linear beam elements. Large deflections and rotations are gradually built and
nonlinear dynamics are introduced by imposing to each sub-body, the deflections and rotations of preceding sub-bodies as
rigid body motions. Dynamic coupling of the sub-bodies is introduced by communicating the reaction loads (3 forces and 3
moments) at the first node of each sub-body to the free node of the previous sub-body as external load.

Rotor aerodynamics in both codes is simulated using a Blade Element Momentum (BEM) model. In hGAST an
15 elaborated BEM model is employed that accounts for dynamic inflow, yaw misalignment, and dynamic stall effect through
the ONERA dynamic stall model (Petot, 1989). In GAST_lin the frozen wake concept is adopted while unsteady
aerodynamics and dynamic stall effect are again accounted for by means of the ONERA model. In the linearized tool, the
unsteady aerodynamic and dynamic stall equations, the corresponding aerodynamic states (circulation parameters of the
ONERA model) and the structural equations along with the corresponding DOFs are treated uniformly in one system
20 following the so-called "Aeroelastic Beam Element" concept (Riziotis et al, 2004). It is noted that the effect of gravity is
neglected in GAST_lin as it is not expected to affect stability characteristics of the wind turbine.

In normal operating conditions stability analysis is performed in the context of multi-blade transformation (Coleman & Feingold, 1958). As already discussed in the introduction section stability analysis of a rotating rotor experiencing yawed inflow would require application of Floquet's theory. This is because periodic coefficients arising from the asymmetry of aerodynamic loads cannot be eliminated by means of Coleman's transformation. However, given that idling speeds are usually small (~1 RPM) and in order to avoid computationally expensive Floquet analysis, stability analysis is performed for a static rotor at different azimuth angles. Azimuth positions in the range [0°, 120°] are considered that correspond to one third of the rotor revolution. Although the rotor is considered static, a free rotation boundary condition is imposed at the generator side in order to approximate as closely as possible idling operation. Also, the average idling rotational speed which has been obtained through the time domain analyses, is taken into account in forming the local to the blade sections velocity triangles and in calculating the induction parameters.

3.2 Description of the ONERA model

As already noted dynamic stall modeling is essential for the consistent computation of the aerodynamic loads of an idling rotor. In this respect, here the extended ONERA model (Petot, 1989) used in hGAST software, as well as its implementation in the aeroelastic tool is described. Furthermore, some validation cases of the model for pitching airfoils are presented at the end of the section.

In the extended ONERA model the aerodynamic loads are split into a potential part (indicated by index 1) and a separated part (indicated by index 2). The lift and drag forces and the twisting moment of a section of the blade are given by the expressions:

$$L = L_1 + L_2 = \underbrace{\frac{\rho c}{2}\left(W_{eff}\ \Gamma_{1L} + \frac{s^L c}{2}\dot{w}_0 + \frac{k^L c}{2}\dot{w}_1 \right)}_{L_1} + \underbrace{\frac{\rho c}{2} W_{eff}\Gamma_{2L}}_{L_2}$$

$$D = D_1 + D_2 = \underbrace{\frac{\rho c}{2}\left(W_{eff}^2 C_{Dlin} + \frac{\sigma^D c}{2}\dot{w}_0 \right)}_{D_1} + \underbrace{\frac{\rho c}{2} W_{eff}\Gamma_{2D}}_{D_2} \qquad (1)$$

$$M = M_1 + M_2 = \underbrace{\frac{\rho c^2}{2}\left(W_{eff}^2 \cdot C_{Mlin} + \frac{(\bar{\sigma}^M + d^M)\cdot c}{2}\dot{w}_0 + \sigma^M W_{eff}\cdot w_1 + \frac{s^M c}{2}\cdot \dot{w}_1 \right)}_{M_1} + \underbrace{\frac{\rho c^2}{2} W_{eff}\cdot\Gamma_{2M}}_{M_2}$$

where ρ is the air density, c is the local blade chord, W_{eff} is the local effective flow velocity at every section of the blade, w_0 is the effective flow velocity component normal to the section chord and w_1 is a rotation velocity parameter due to torsion (both velocity components are explained in Figure 8) given by:

$$w_0 = W_{eff}\sin\alpha_{eff}$$

$$w_1 = \frac{c}{2}\dot{\theta}_y \qquad (2)$$

α_{eff} is the local flow incidence and θ_y is the local torsion angle of the section (dot denotes differentiation with respect to time). In (1), Γ_{1L} and Γ_{2L} are two circulation components (normalized by the semi-chord $c/2$) that define lift force. The first one corresponds to attached flow (potential flow lift) while the second provides a necessary correction to account for the effect of flow separation (correction due to stall). Similarly, Γ_{2D} and Γ_{2M} are two "equivalent" circulation components for

5   the calculation of the correction due to flow separation on the drag and the twisting moment respectively. C_{Dlin} and C_{Mlin} are explained in Figure 9 and finally, s^L, k^L, σ^D, $\bar{\sigma}^M$, d^M, σ^M and s^M are parameters of the model. Expressions of all model parameters are provided at the end of the section.

It is noted that L_1 and M_1 definitions in (1) are consistent with Theodorsen's model description for a pitching and plunging airfoil section. The first term of the L_1 equation is the circulatory lift component; the second term is the added mass

10   contribution due to plunging motion (mainly due to flapping motion); and the third term is the added mass contribution due to the section pitching motion (torsion rotation). Similar circulatory and added mass contributions appear in M_1 equation.

The two equivalent circulation parameters of the lift force Γ_{1L} and Γ_{2L} are defined through the solution of a first and a second order differential equations respectively:

$$\dot{\Gamma}_{1L} + \frac{\lambda^L}{\tau}\Gamma_{1L} = \frac{1}{2}\frac{\lambda^L}{\tau}\left(\frac{dC_L}{d\alpha}\right)_{\text{lin}} W_{\text{eff}} \sin\left[2(\alpha_{\text{eff}} - \alpha_0)\right] + \frac{\lambda^L}{\tau}\sigma^L w_1 + \left(\alpha^L\left(\frac{dC_L}{d\alpha}\right)_{\text{lin}} + d^L\right)\dot{w}_0 + \alpha^L\sigma^L\dot{w}_1$$

(3)

$$\ddot{\Gamma}_{2L} + \frac{a^L}{\tau}\dot{\Gamma}_{2L} + r^L\frac{\Gamma_{2L}}{\tau^2} = -\left[\frac{r^L}{\tau^2}W_{\text{eff}}\left(\Delta C_L\right) + \frac{E^L}{\tau}\dot{w}_0\right]$$

The equivalent circulation parameters of the drag force Γ_{2D} and pitching moment Γ_{2M} are defined through the solution

15   of two second order differential equations (similar in form to the equation for Γ_{2L}):

$$\ddot{\Gamma}_{2D} + \frac{a^D}{\tau}\dot{\Gamma}_{2D} + r^D\frac{\Gamma_{2D}}{\tau^2} = -\left[\frac{r^D}{\tau^2}W_{\text{eff}}\left(\Delta C_D\right) + \frac{E^D}{\tau}\dot{w}_0\right]$$ (4)

$$\ddot{\Gamma}_{2M} + \frac{a^M}{\tau}\dot{\Gamma}_{2M} + r^M\frac{\Gamma_{2M}}{\tau^2} = -\left[\frac{r^M}{\tau^2}W_{\text{eff}}\left(\Delta C_M\right) + \frac{E^M}{\tau}\dot{w}_0\right]$$ (5)

In (3), $\left(\dfrac{dC_L}{d\alpha}\right)_{\text{lin}}$ is the slope of the linear part of the $C_L - \alpha$ curve, $\left(\Delta C_L\right)$, $\left(\Delta C_D\right)$ and $\left(\Delta C_M\right)$ are differences of the real steady-state viscous lift, drag and moment coefficients from their "linear" counterparts at α_{eff} as explained in Figure 9, τ is a time parameter given by $\tau = \dfrac{c}{2W_{\text{eff}}}$, and λ^L, σ^L, α^L, d^L, a^L, r^L, E^L, a^D, r^D, E^D, a^M, r^M, E^M are parameters of the model with, $a^\ell, r^\ell, E^\ell = f\left(\Delta C_L^2\right)$, $\ell = L, D, M$.

Expressions of all model parameters appearing in equations (1), (3), (4) and (5) are given below as functions of the model constants. Compressibility of the flow is taken into account through the expression of various parameters as functions of the ocal flow Mach number M defined with respect to W_{eff} :

$$s^L = \pi + 5\pi[(1-M^2)^{0.285} - 1] \quad , \quad k^L = \frac{\pi}{2} + 1.96\pi\left(\sqrt{1-M^2} - 1\right)$$

$$\lambda^L = 0.17 - 0.13M \quad , \quad \alpha^L = 0.53 + 0.25(\sqrt{1-M^2} - 1),$$

$$\sigma^L = 2\pi / (\sqrt{1-M^2}) \quad , \quad d^L = \sigma_1^L \left|\Delta C_L\right|$$

$$\sigma^D = \sigma_0^D \cdot \alpha_{eff} + \sigma_1^D \left|\Delta C_L\right|$$

$$s^M = -\frac{3\pi}{16} \cdot [-1.26 - 1.53 \cdot \tan^{-1}(15 \cdot (M - 0.7))] \quad , \quad \sigma^M = \sigma_0^M + \sigma_1^M \left|\Delta C_L\right|$$

$$\sigma_0^M + s^M = -\frac{\pi}{2} \cdot [1 + 1.4 \cdot M^2] \quad , \quad \bar{\sigma}^M = -\frac{\pi}{4} \cdot [1 + 1.4 \cdot M^2]$$

$$d^M = \sigma_1^M \cdot \left|\Delta C_L\right|$$

$$\sqrt{r^\ell} = r_0^\ell + r_2^\ell \Delta C_L{}^2, \quad a^\ell = a_0^\ell + a_2^\ell \Delta C_L{}^2, \quad E^\ell = E_2^\ell \cdot \Delta C_L{}^2, \quad \ell = L, D, M$$

For the constants of the ONERA model, ranges are proposed in Petot (1989). The selected values of the constants depend on the airfoil geometry and they should be tuned separately for every different airfoil shape. Since we usually lack of measured unsteady aerodynamic data for the different airfoils of the blade (that could be used for the tuning of the constants), fixed values are defined in hGAST, lying within the ranges proposed by Petot which give reasonable results for most airfoils. They have been down selected through a tuning process that has been performed based on several unsteady measurements on pitching airfoils of various geometries (Riziotis, 2003) (some examples are shown in the sequel) and they are reported in Table 1.
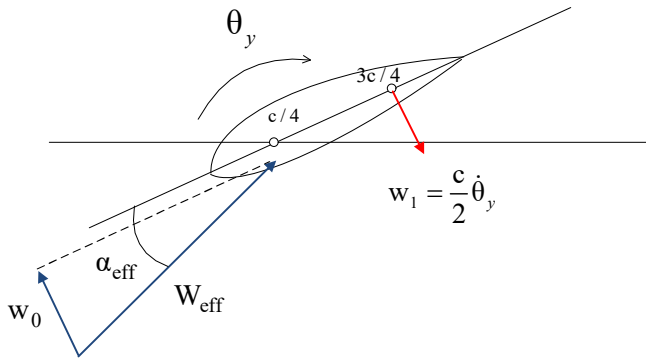
Figure 8. Definition of local velocity components of ONERA model.
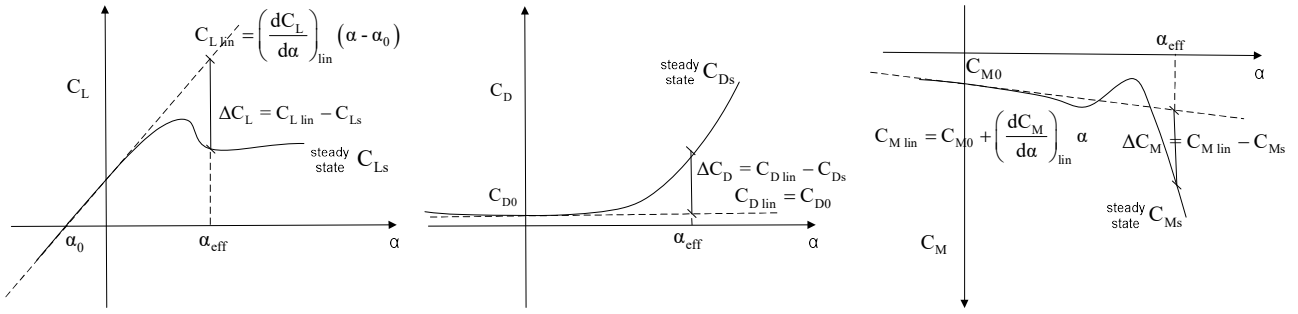
Figure 9. Static polar depended parameters definitions in ONERA model.

Lift constant	Drag Constants	Pitching Moment Constants
$\sigma_1^L = 0$	$\sigma_0^D = 0.172, \quad \sigma_1^D = 0$	$\sigma_1^M = 0$
$r_0^L = 0.18, \quad r_2^L = 0.18,$	$r_0^D = 0.22, \quad r_2^D = 0.2$	$r_0^M = 0.22, \quad r_2^M = 0.20$
$a_0^L = 0.3, \quad a_2^L = 0.2,$	$a_0^D = 0.25, \quad a_2^D = 0$	$a_0^M = 0.25, \quad a_2^M = 0.05$
$E_2^L = -1.5$	$E_2^D = -1.15$	$E_2^M = 1.425$

Table 1. ONERA model constants used in hGAST.

5   In the sequel, results of the ONERA model are presented and compared against wind tunnel measurements for airfoils undergoing pitching motion at high angles of attack. Pitching motion is defined through the equation $a = \alpha_0 + a_1 \sin(\omega t)$ where α_0 is the mean angle, α_1 is the amplitude and ω is the angular velocity of the periodic motion. Given the chord length c of the section and the free stream velocity U_∞ the dimensionless reduced frequency parameter $k = \omega c / 2U_\infty$ is defined. Along with the results of the ONERA model predictions of the state-of-the-art Beddoes-Leishman (BL) model used

10   in several aeroelastic design tools as baseline dynamic stall model are also presented (implementation by Hansen et al, 2004). In this way, performance capabilities and limitations of the two models (ONERA and Beddoes-Leishman) are highlighted.

     The first set of cases concerns NACA 63415 airfoil while the second set concerns FFA-W3-241 airfoil (this is the airfoil used in the outer part of the DTU Reference Wind Turbine blade). They have been both tested by DTU in VELUX open jet

15   wind tunnel at a Reynolds number of $Re = 1.6 \times 10^6$ and a Mach number of $M = 0.12$. The test campaign data are reported in Bak et al (2000) and Fuglsang et al (1998) respectively. Although the above tests are relatively old, they are well suited for the purposes of the present study because they correspond to operation within stall regime. Usually, dynamic stall tests run from fully attached to fully separated flow conditions over one period of oscillation. This is not representative of the dynamic stall conditions encountered by an idling blade. The idling blades experience high AOA variations over the period

20   of their rotation (low frequency variations) but small amplitude oscillations over periods related to their natural frequencies.

So, the above tests, of low amplitude oscillations, match very well the conditions encountered by the idling blade as well as the work simulations performed for the identification of the nonlinear damping characteristics of the rotor. Another point of discussion could be that the above tests correspond to a pitching motion and not to a combined heaving/translation motion as one expects to have on an idling blade (blade undergoing flap-edge motion). However, to the authors' knowledge no such tests exist at least for very high AOA.
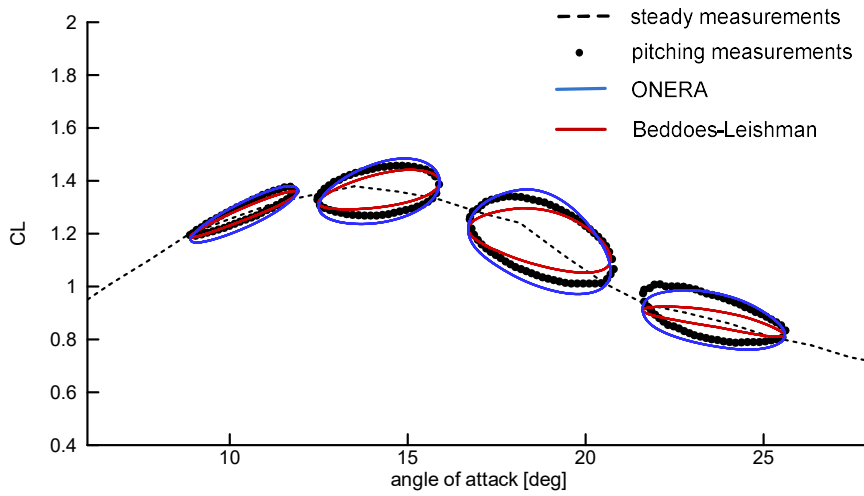
Figure 10. Comparison of engineering dynamic stall models against measurements. Results for a pitching NACA 63415. Mean angles of the four cases $\alpha_0 = 10.4^0, 14.2^0, 18.7^0, 23.6^0$, amplitudes of the four cases $\alpha_1 = 1.5^0, 1.7^0, 2^0, 2^0$, reduced frequency $k = 0.09$ (Bak et al, 2000).
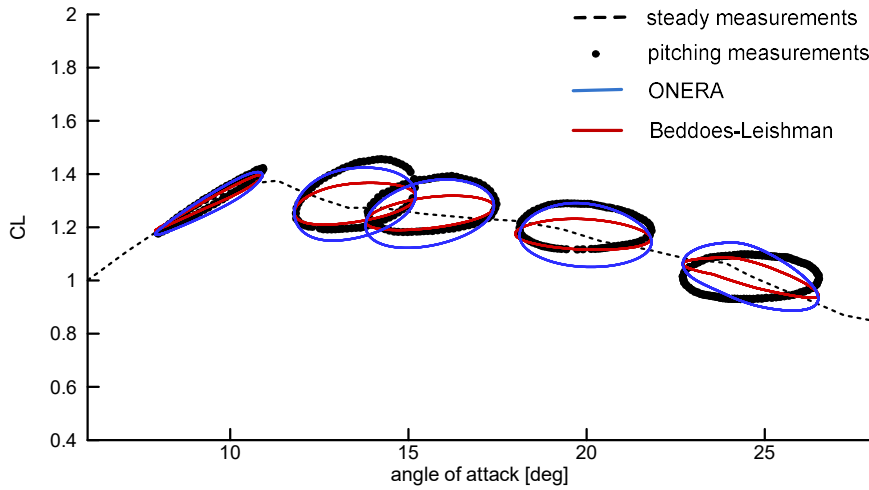
Figure 11. Comparison of engineering dynamic stall models against measurements. Results for a pitching FFA-W3-241. Mean angles of the five cases $\alpha_0 = 9.4^0, 13.5^0, 15.6^0, 19.9^0, 24.6^0$, amplitudes of the five cases $\alpha_1 = 1.5^0, 1.7^0, 1.8^0, 1.9^0, 1.9^0$, reduced frequency $k = 0.093$ (Fuglsang et al, 1998).

The cross comparison shows that overall both models perform well, even in deep stall conditions. It is seen that BL model better predicts the width of the dynamic stall loops in light stall conditions (α_0 angles below C_{Lmax} angle). In these light stall cases ONERA model seems to slightly over-predict the width of the re-attachment region especially for NACA airfoils. For the same airfoil ONERA model better predicts the width and the slope of the loops in the deep stall region (beyond C_{Lmax} angle). For the FFA-W3-241 airfoil both models seem unable to correctly predict the slope of the loops especially at higher mean angles. They both predict lower slope which is a clear indication of aerodynamic damping underestimation. ONERA model predicts higher and BL model lower width of the dynamic stall loops in deep stall as compared to measurements. What is clearly seen in all comparisons is that at very high AOA (highest α_0 angle) BL model considerably under predicts the width of the loops while ONERA consistently provides reasonable results even at these extreme dynamic stall conditions. The above behaviour of BL model is due to its feature to automatically switch to almost steady-state aerodynamics at very high AOA (well beyond C_{Lmax} AOA) (see Hansen et al, 2004) while ONERA model is fully deployed at all AOA.

Despite the reasonable agreement obtained in the above presented cases, it is not straightforward to support that ONERA model is fully validated in deep stall conditions. Apparently, no dynamic stall model yet exists that is thoroughly validated in deep stall and this is mainly because of the lack of relevant measured data of combined heaving-translation motion that could serve its tuning.

By definition, the ONERA model makes no distinction in the treatment of dynamic stall between positive and negative AOAs. The correction of the potential lift is made on the basis of $\Delta C_L, \Delta C_D, \Delta C_M$ which at negative AOA stall are defined in a similar manner as at positive. The model has already been tested in VAWT applications and for low tip speed ratio values, where blades go into negative AOAs stall on the advancing side and positive AOA stall on the retreating side, predictions of aerodynamic loads have been proved to be in good agreement with measurements (see Shi et al, 2014). This isimportant, since in idling operation the blades experience AOA in both regimes. Thereby, it can be stated that the model functions are equally well suitable at negative stall conditions.

For the eigenvalue stability analysis of the rotor/wind turbine system, aerodynamic loads of equation (1) and ONERA differential equations (3), (4) and (5) are linearized analytically and combined with the beam equations in one set that is solved using FEM method in the context of the so called "Aeroelastic Beam Element" approach. Therefore, additional mass, damping and stiffness matrices are obtained through the linearization of the aerodynamic loads that supplement the structural ones.

4   Results and discussion

4.1 Time-domain analysis results

Time domain aeroelastic simulations in turbulent inflow are performed for the Reference 10 MW wind turbine, at a mean wind speed of 42.5 ms^{-1}, with a turbulence intensity (TI) 11%, for various yaw misalignment angles in the range [-60°, +60°] and constant pitch angle of 87°. Six 10-minute simulations are performed for every yaw angle corresponding to different realizations of the wind (wind seeds). Figure 12 presents the min-max envelope of the edgewise (out-of-plane) bending moments at blade root as functions of the yaw misalignment angle. Load results of all three blades for the different wind seeds, as well as average loads are provided in the plot. It is seen that ultimate loads attain both maximum and minimum value at +30° of yaw. When loads are averaged, the minimum is found at +22.5^o of yaw (very close though to the load at +30° of yaw) while the maximum is still obtained at +30° yaw angle.
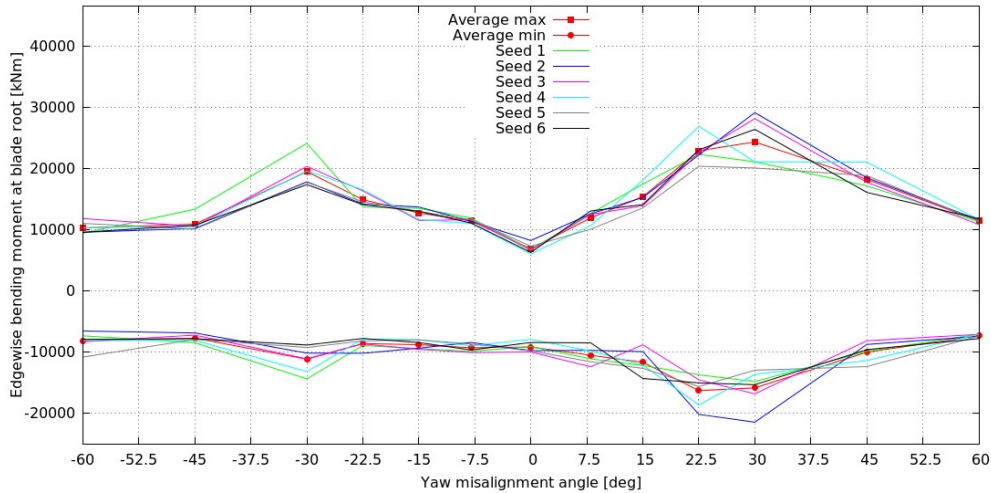
Figure 12. Ultimate blade root edgewise bending moments. Loads from 6 wind seeds are averaged. Wind speed 42.5 ms^{-1}; TI=11%; yaw angles in the range [-60°, +60°].

For the yaw angle of 30° a pattern of the edgewise bending moments at the three blade roots is shown in Figure 13 along with the time series of the azimuth angle and the AOA for a 45s duration. The average idling speed of the rotor is about 0.8 RPM at the above conditions (wind speed 42.5 ms^{-1} and yaw 30°). Also in Figure 14, the obtained C_L values at r/R=90% are collected and plotted with respect to the corresponding AOA. In this plot, the regions of unfavourable lift slope are marked in grey.

At t=107s (marked with a dashed blue line in Figure 13), mild edgewise vibrations start to grow on blade 3 as a result of increasing AOAs that push the blade into stall. At t=107s rotor azimuth is 90° (rotor azimuth is defined as the azimuth angle of the blade that lies in the sector [0°, 120°] – blade 1 in this case). It is noted that 0° azimuth corresponds to a blade being at 12 o'clock. The AOA on blade 3 crosses the level of 15° so stall takes place at positive AOA. Blade 2 also operates in deep stall experiencing negative AOA in the range [-30°, -40°]. Finally, the flow remains attached on blade 1. The AOAs

experienced by blade 1 remain at about -10° AOA for approximately 5 s and so no vibrations are expected for this blade within this time interval.

Progressing in time, the situation is changing. At t=116 s (marked by a red dashed line), mild edgewise vibrations now start to grow on blade 1 as a result of increasing AOA that push this blade into stall at the negative AOAs regime. As indicated in Figure 13, at t=116 s, the azimuth angle of the rotor is 20° and the AOA "seen" by blade 1 grows to about -30°. As time evolves (time period [116 s,120 s]), blade 1 goes deeper into negative AOA stall (about -40°) while over the same time period, blade 3 stays within deep stall experiencing AOA in the range [20°, 30°]. This explains why blade 3 exhibits large vibrations over the whole time period [107 s, 120 s]. Return to attached flow conditions is only obtained for blade 3 at t>120 s. Opposite to the other two blades, now blade 2 operates in attached flow conditions (AOA~ -15°).

Looking back in time, at the time interval [80 s, 95 s], it can be seen that blade 1 is experiencing similar flow conditions to those experienced by blade 3 in the time interval [107 s, 115 s]. Blade 2 is now lying in the azimuth range of [80°, 100°]. The only difference with respect to the time period [107 s, 115 s] is that now the rotor speed is lower and therefore blade 1 remains longer within the stall region. High load amplitudes are obtained for blade 1 within this time interval, which decrease when blade 1 moves away from stall (AOA and loads of blade 1 decrease in the time interval [95 s, 105 s]).

4.2 Eigenvalue analysis results

In the present section eigenvalue stability analysis results for the idling rotor are presented at the wind velocity of 42.5 ms⁻¹ and for various yaw angles in the range [0°, 60°]. The average idling speed versus yaw angle in the stability analysis was taken from the time domain simulation results by averaging the mean rotor speed of the six realizations performed for every yaw angle. The results of the mean idling speed as function of the yaw angle are shown in Figure 15. Emphasis is put on yaw angles for which higher minimum/maximum loads are predicted by nonlinear time domain analysis. A correlation is attempted between the damping and frequency predictions obtained through the eigenvalue stability analysis with the results of the time domain analysis. Eigenvalue stability analysis is performed using both steady-state and unsteady (ONERA model) aerodynamics. The feature of BL model to automatically switch to steady-state aerodynamics at very high AOA necessitated the analysis with steady state polars. Given that within stall region damping predictions of the steady-state analysis will be the most conservative, by using steady-state polars the range of anticipated damping predictions can be determined.

The modal frequencies and damping (in logarithmic decrement) of the rotor modes (M3-M8) at 0° yaw are shown in Figure 16(a)&(b) as functions of the rotor azimuth angle in the range of [0°, 120°] (azimuth angle of blade 1). Results are obtained using ONERA unsteady aerodynamics model. In Figure 17(a)&(b) the PSDs of the flapwise and edgewise bending moments coming from the earlier presented time domain simulations are also provided for the same yaw angle.
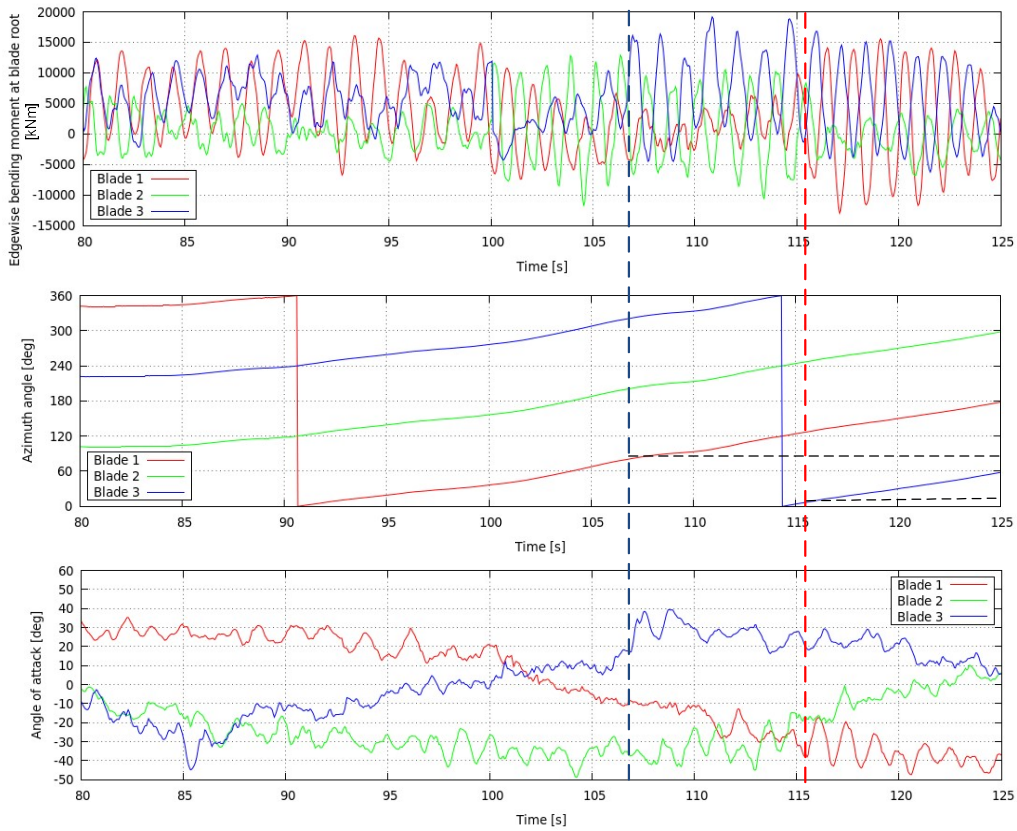
Figure 13.Times series of blade root edgewise bending moment, blade azimuth angle and angle of attack at r/R=0.90 spanwise position. Wind speed 42.5 ms⁻¹, TI 11%, yaw angle 30°.
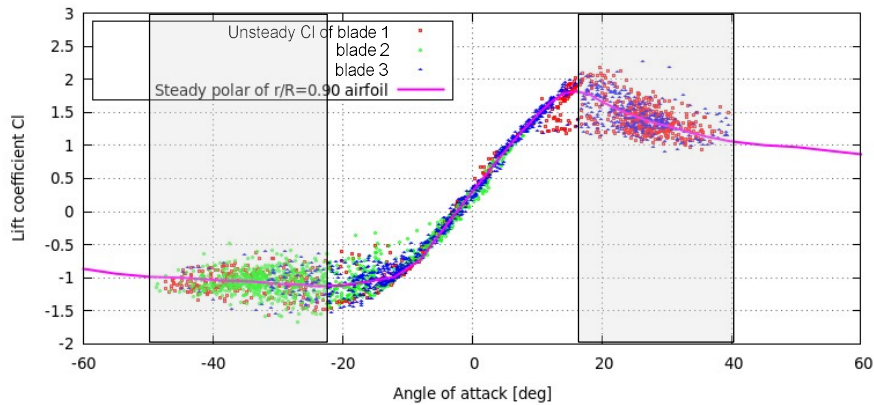
5   **Figure 14.CL - AOA plot at r/R=0.90 spanwise position. Wind speed 42.5 ms⁻¹, TI 11%, yaw angle 30°.**

It is seen that the three out-of-plane modes, M5, M6 and M7, are clearly the lowest damped ones (Figure 16(b)). This is definitely in agreement with the time domain analysis results as shown in the PSD plots of the edgewise bending moment at

the root of the three blades (Figure 17(b)). The three predominant peaks on the PSD plot indicate the modes that are highly excited. The corresponding frequencies are found at ~0.69 Hz, 0.81 Hz, 0.95 Hz. These frequencies agree well with the values obtained with the stability tool (Figure 16(a)). A lower peak appears at 0.25 Hz which corresponds to the first longitudinal tower bending mode M1. On the contrary no peak appears in the PSD of the blade root flapwise bending

5   moment (Figure 17(a)). This indicates that the aerodynamic damping of the in-plane modes M3, M4 and M8 is high. The same result is consistently predicted by the stability tool (all values are above 100% in logarithmic decrement). Worth noticing is that both the level of damping and the frequencies are almost independent of the azimuth position in the 0° yaw case. Eigenvalue analysis using steady-state polars (not shown in the figures) gives similar results with those of the unsteady aerodynamic analysis. The damping of the low damped out-of-plane (edgewise) modes M5, M6 and M7 remains positive at

10 all azimuth angles while in-plane (flapwise) modes appear to have about 50% higher damping and 20% lower frequency. The damping and frequencies are almost independent of the azimuth angle also when steady-state aerodynamics is used.

Figure 18(a) & (b) present frequency and damping results for the yaw angle of 30° using steady-state aerodynamics. The same set of results using unsteady aerodynamics is presented in Figure 19(a)&(b). Figure 20(a)&(b) give the PSDs of the flapwise and edgewise bending moments at the blade root of the three blades as predicted through nonlinear time domain

15 simulations. It is reminded that according to the time domain analysis results of Sect. 4.1, at 30° yaw the edgewise loads reach their maximum values. Also, as explained in Sect. 2, for this high yaw angle the AOAs experienced by the rotating blades will significantly vary with the azimuth angle. As a result, modal frequencies and damping also vary over the revolution in contrast to the 0° yaw case. At very high yaw angles, the AOAs seen by the blades are expected to enter post stall on both sides of the polar (positive and negative AOAs).
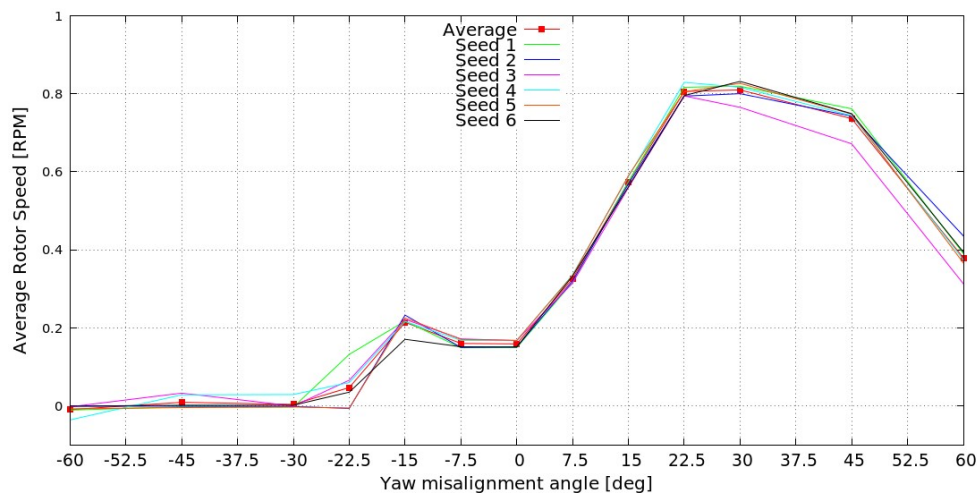
Figure 15. Rotor idling speed vs. yaw angle for the pitch angle of 87°. Average rotor speed of six different 10 min wind seeds and their average.
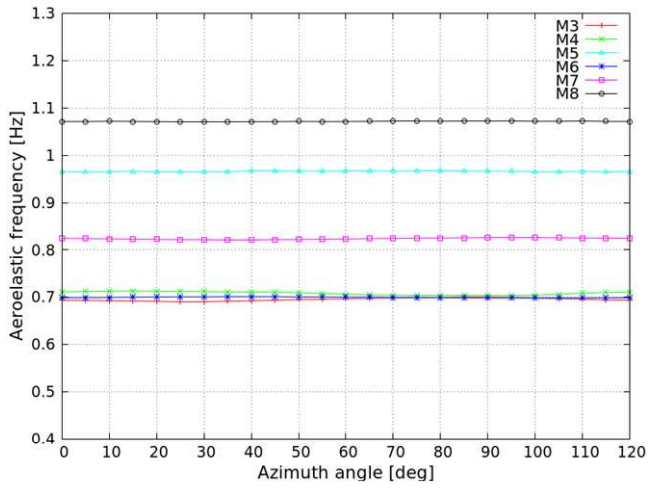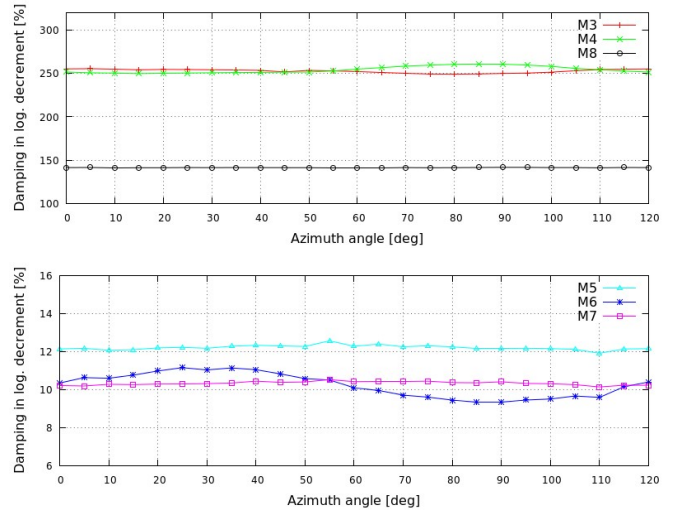
Figure 16. (a) Modal frequency& (b) modal damping of rotor modes vs. azimuth angle, at U=42.5 ms⁻¹ and yaw=0° (Unsteady aerodynamics based on ONERA model).
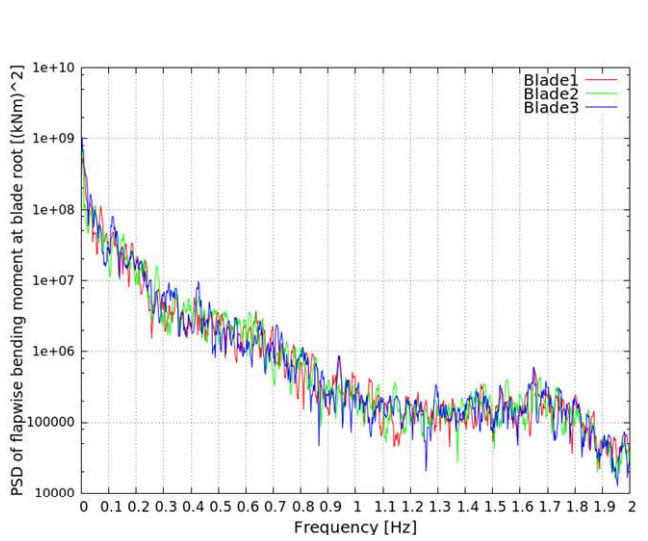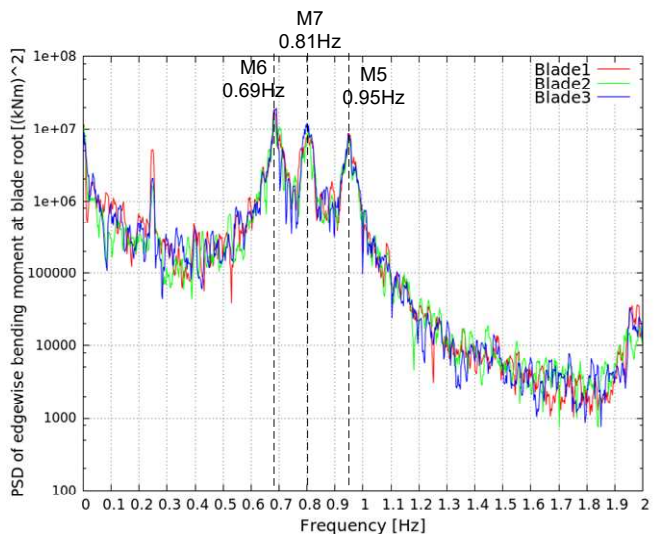
Figure 17. (a) PSD of the flapwise bending moment at the blade root& (b) PSD of the edgewise bending moment at the blade root, at U=42.5 ms⁻¹ and yaw=0°.

As compared to the 0° yaw case, lower damping values are obtained for most modes (in-plane and out-of-plane). This indicates that stall induced vibrations start to develop at the yaw angle of 30°. The damping of the in-plane modes M3, M4 and M8 significantly drops. The damping of M4 (asymmetric flap tilt/horizontal mode) becomes even negative at certain azimuth angles. When steady-state polars are used, the damping of M4 is negative at the azimuth ranges [0°,25°] and [75°,120°]. Almost constant, high negative damping values of about -25% are obtained for M4 in the above azimuth ranges. When ONERA unsteady aerodynamic model is used the damping becomes locally negative only at the azimuth angles of 0° and 100°. Despite the negative damping values of M4, damping remains highly positive (up to 150%) over a wide azimuth range of [30°,70°]. This suggests that the overall damping of the in-plane modes will be eventually positive. On the other hand, modes M5, M6, M7 still have low or negative damping throughout the entire range of azimuth angles. Especially for M7 (asymmetric edge horizontal/tilt mode) the damping is negative at all azimuth angles both for steady-state and unsteady aerodynamics. Comparing the two aerodynamic models, the damping of M7 is lower at all azimuth angles when steady state-polars are used. For M5 and M6 the damping predicted with unsteady aerodynamics remains low but positive at all azimuth angles while with steady-state aerodynamics the damping is negative in the azimuth ranges [0°,20°] and [90°,120°].

The stability results that used unsteady aerodynamic modeling are in line with the observations made in the time domain analysis of the previous section. In agreement with the time domain analysis results, higher negative damping values are noted over the azimuth ranges [0°, 20°] and [75°, 110°] (azimuth ranges where higher vibrations have been observed in time domain results). Again, four peaks dominate the PSD plot of the edgewise bending moment at 0.25 Hz, 0.7 Hz, 0.8 Hz and 0.95 Hz (see Figure 20(b)). The first one corresponds to the first tower longitudinal bending mode M1 while the other three correspond to the three edgewise (out-of-plane) modes M5, M6, M7. Again, the frequencies of the highly excited modes in the results of the time domain analysis agree well with the frequencies predicted by the stability tool (Figure 19(a)) for the low damped rotor out-of-plane modes. The largest peak is seen at the frequency of 0.8 Hz (the frequency of M7) indicating that indeed this is the lowest damped mode of the rotor. A closer look in the vicinity of the 0.8 Hz peak (see focus plot Figure 21(a)) reveals two additional peaks around the centre frequency of 0.8 Hz with a frequency shift of about $\pm 0.01\,\text{Hz}$.

The above frequency shift corresponds to the average idling rotational frequency (1p frequency). These peaks represent rotating periodic dynamics of the system (in terms of the principle eigenfrequency) and they are found to be even more excited than the centre frequency peak. Such peaks are not observed in the PSD plot of the 0° yaw case since the idling speed of the rotor is almost zero in this case, as seen in Figure 15. In a simulation with uniform inflow, at the same wind speed (42.5 ms^{-1}), the abovementioned peaks become more distinct (other peaks appear as well that correspond to higher multiples) as seen in the PSD plot of Figure 21(b). It is noted that in the uniform inflow case, after an initial transient, the idling speed reaches a constant value (0.78 RPM, 0.013 Hz). This explains why the two peaks appear at frequencies exactly equal to $\pm \omega$ of the principle eigenvalue. In the case of turbulent wind, the idling speed continuously changes and therefore the obtained peaks are more spread. The amplifying response of the edgewise moment in the simulation with uniform inflow shown in Figure 22 indicates that under uniform inflow conditions the system is unstable. The above result is in perfect agreement with the results of the eigenvalue analysis which show that M7 mode is negatively damped at all azimuth angles. In turbulent

wind simulations instabilities are mitigated as a result of the incoherent loading of the blades along their span and the continuous variation of the inflow that pushes the blade in and out stall (regions of negative C_L slope).

In Figure 20(a) high energy levels are noted in the frequency range of [0.5 Hz, 0.6 Hz]. The peak corresponds to the in-plane mode M4. As discussed earlier, according to the stability predictions, this is the lowest damped flapwise mode. The smooth shape and the spread of the peak indicate the high aerodynamic damping involved.
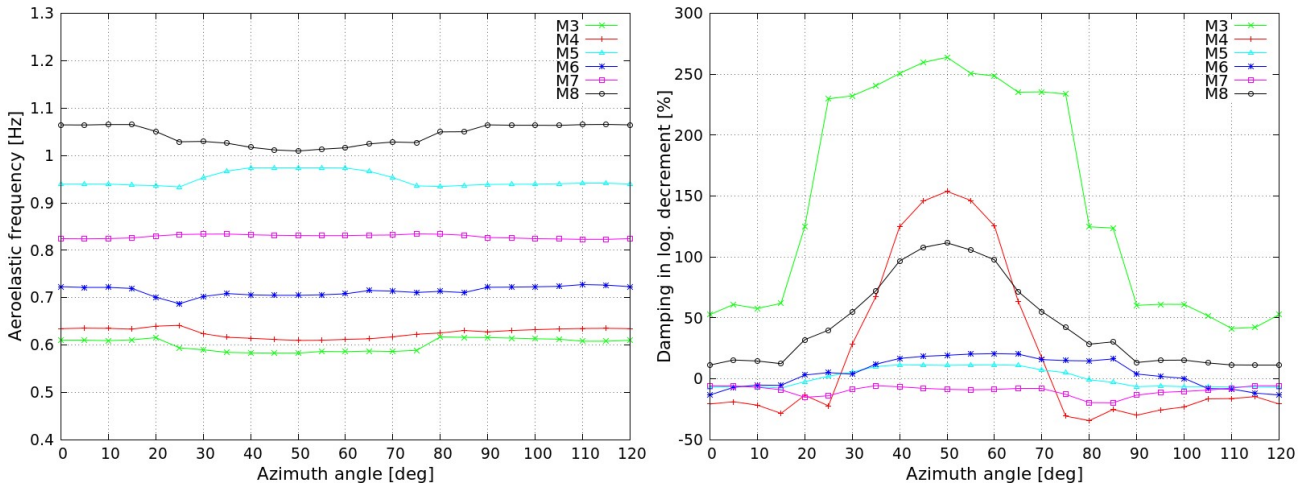
Figure 18. (a) Modal frequency & (b) modal damping of rotor modes vs. azimuth angle, at U=42.5 ms^{-1} and yaw=30° (Steady-state aerodynamics).

(a)   (b)
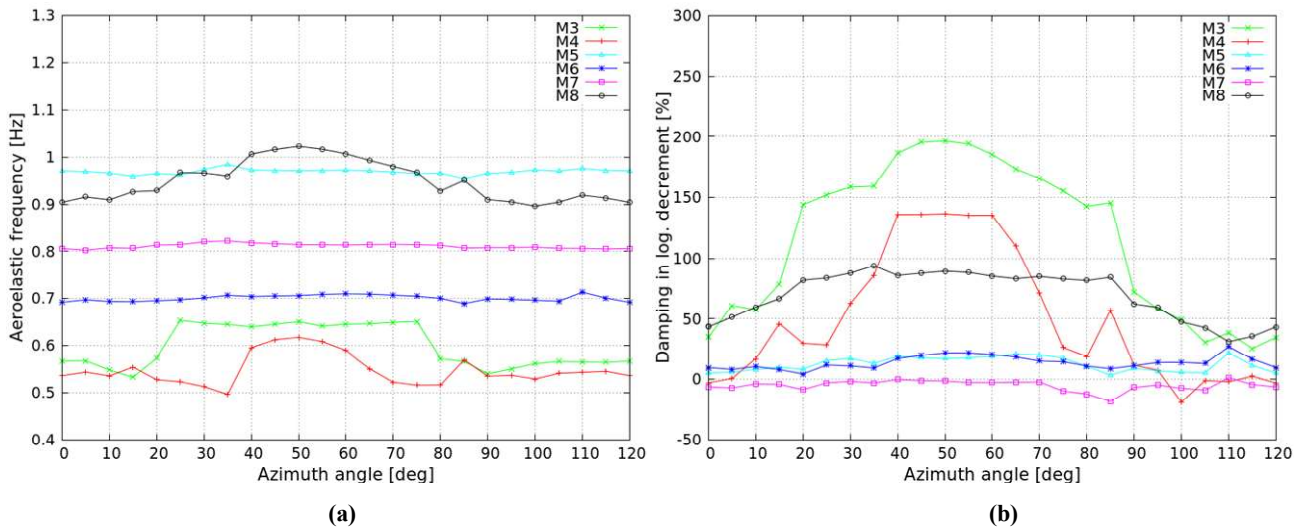
Figure 19. (a) Modal frequency & (b) modal damping of rotor modes vs. azimuth angle, at U=42.5 ms^{-1} and yaw=30° (Unsteady aerodynamics based on ONERA model).

(a)   **(b)**
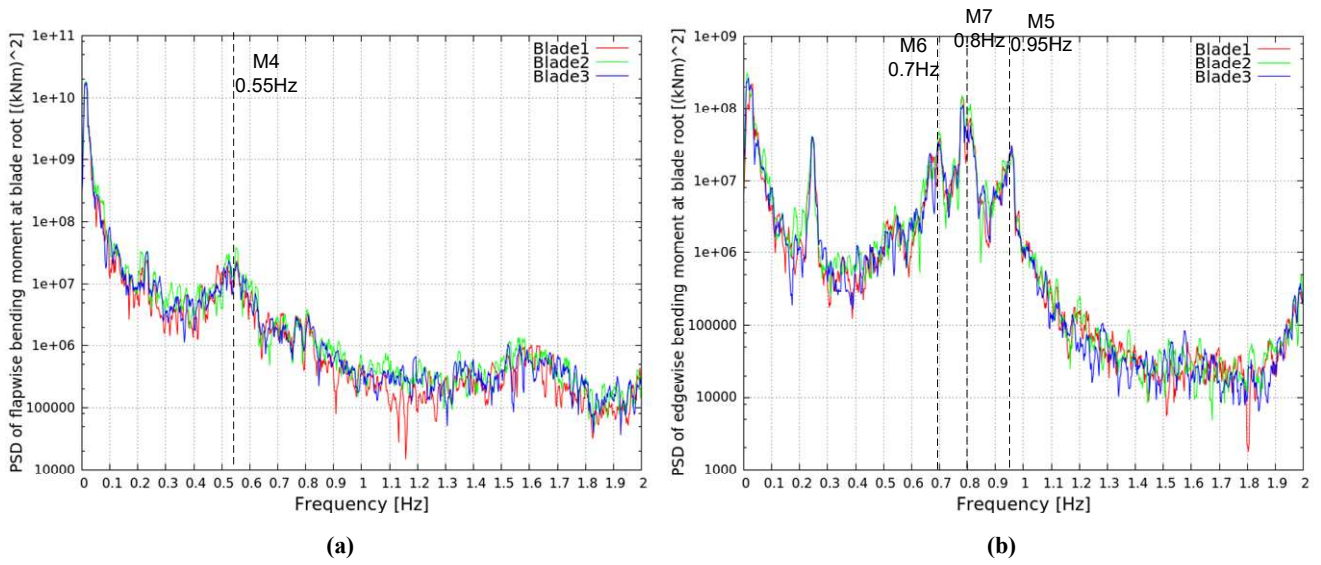
Figure 20. (a) PSD of the flapwise bending moment at the blade root & (b) PSD of the edgewise bending moment at the blade root, at U=42.5 ms⁻¹ and yaw=30°.

(a)   **(b)**
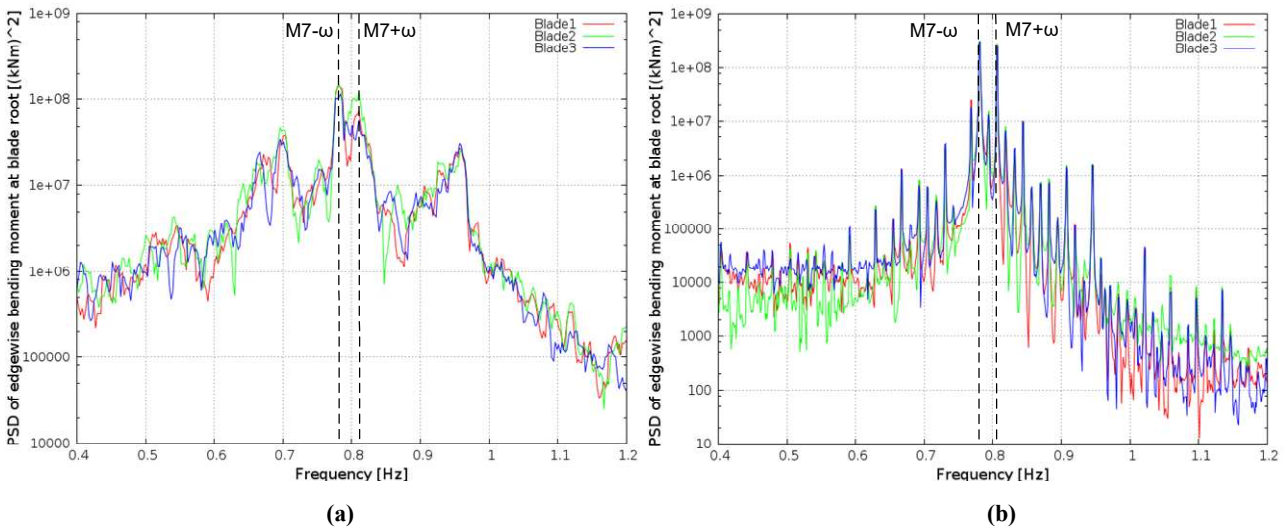
Figure 21. PSD of the edgewise bending moment at the blade root, at U=42.5 ms⁻¹ and yaw=30°(a) Turbulent inflow(focus plot)& (b) Uniform inflow (focus plot).
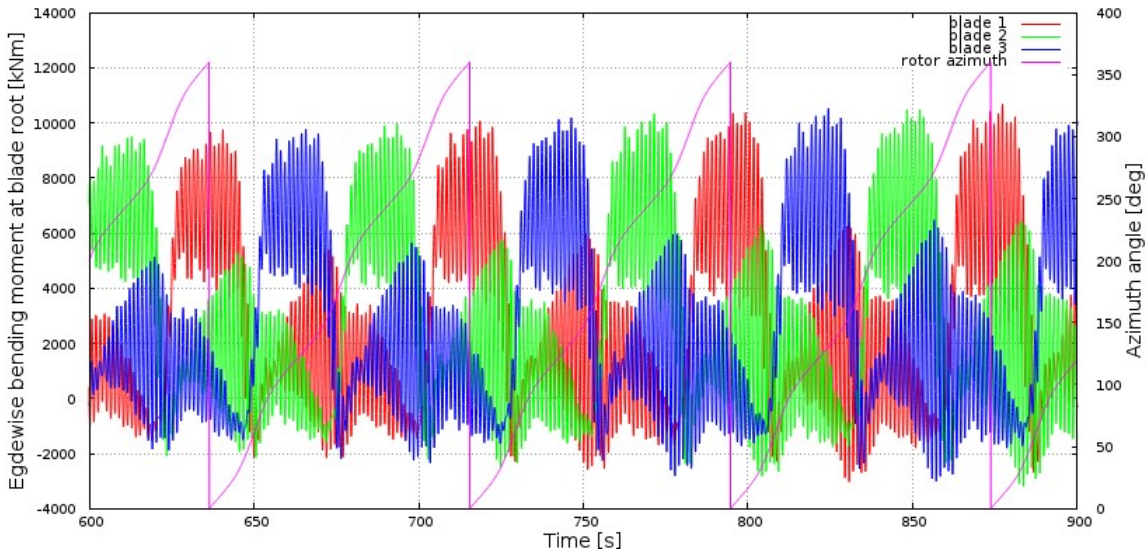
Figure 22.Time series of the edgewise bending moment at the blade root, with uniform inflow at U=42.5 ms⁻¹ and yaw=30°.

In Figure 23 and Figure 24 the damping results for the 45° and 60° yaw cases are shown. Results for both steady and
unsteady aerodynamics are compared. For yaw angles higher than 30° the system stability is gradually restored. This is in
agreement with the results of the time domain analysis which showed a gradual decrease of the edgewise loads beyond the
30° yaw angle. At the yaw angle of 45° (see Figure 23) the damping of M7 increases as compared to the 30° yaw case. The
damping as predicted with steady-state aerodynamics is negative but very close to zero for all azimuth angles while unsteady
aerodynamic analysis always gives positive damping. The lowest damped mode, both with steady and unsteady
aerodynamics, appears now to be M6 (asymmetric edge vertical/yaw mode). Negative values are obtained in the azimuth
range $[105^o,120^o]$ (also in the range $[0^o,10^o]$ with steady-state aerodynamics). The damping of M4 appears to have a negative
dip at 55° azimuth angle in the steady-state results which is smeared out in unsteady computations. Overall the damping of
the in-plane modes seems to decrease as the yaw angle increases however still remains highly positive over a wide range of
azimuth angles.

Damping results at the yaw angle of 60° using steady-state aerodynamics (see Figure 24(a)) are found to be very similar
to those of the 45° yaw case. Unsteady results (see Figure 24(b)) indicate that the damping of M7 continues to increase as the
yaw angle increases. The same holds with mode M6. It is noted that all out-of-plane modes are positively damped at 60° of
yaw while M6 is the mode with the lowest damping characteristics.

(a)   **(b)**
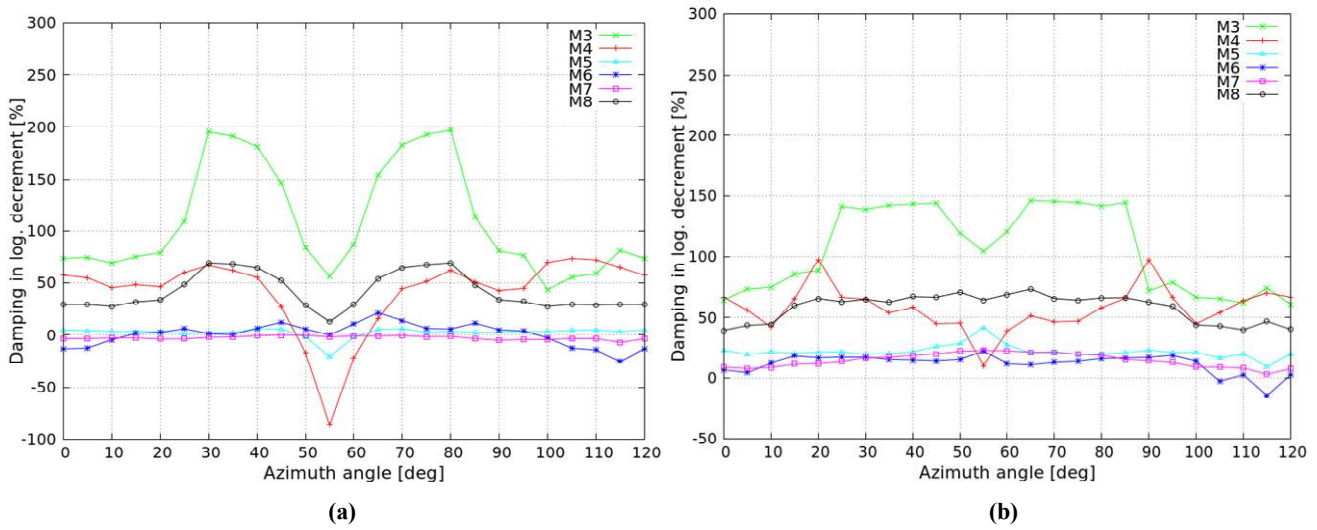
Figure 23.Modal damping of rotor modes vs. azimuth angle at U=42.5 ms⁻¹ and yaw=45° (a) Steady-state aerodynamics (b) unsteady aerodynamics (ONERA modeling).

(a)   **(b)**
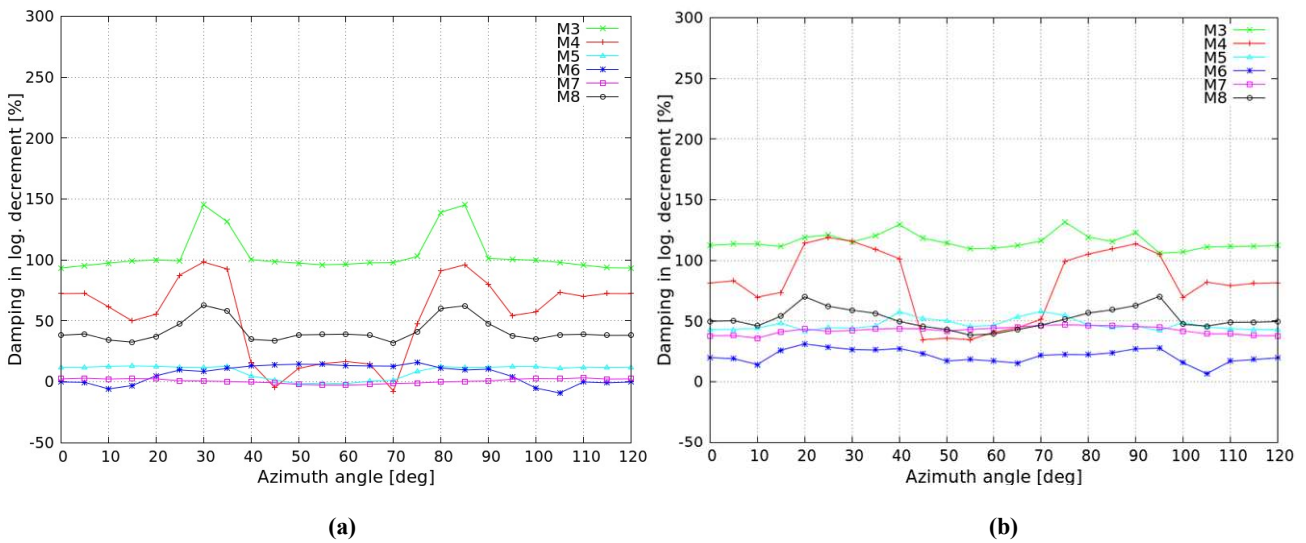
Figure 24.Modal damping of rotor modes vs. azimuth angle at U=42.5 ms⁻¹ and yaw=60° (a) Steady-state aerodynamics (b) unsteady aerodynamics (ONERA modeling).

4.3   Work computation results

Next, the results of the eigenvalue analysis of the previous section are further evaluated by computations of the work of the aerodynamic forces in imposed harmonic vibrations. The blade is subjected to an externally imposed harmonic motion following the shape and frequency of the mode considered and the unsteady aerodynamic loads are calculated along its span at various stations. Then the work done by the aerodynamic loads is computed over one cycle of the blade oscillation. The above work is directly associated with the damping of the corresponding mode. The mode shapes and eigenfrequencies used

in the present analysis are the aeroelastic ones obtained through the eigenvalue analysis on the full aeroelastic system. As opposed to the structural mode shapes (obtained for the free vibration problem in vacuum conditions), the aeroelastic mode shapes also include the phase shift between the various components of the blade motion and therefore provide more realistic prediction of the work distribution.

5   Work analysis is able to bring more insight into stability computations because it provides stability characteristics separately for each blade. When eigenvalue analysis gives negative damping value for a specific mode, work analysis can identify which blade is responsible for the instability as well as the spanwise extent of the negative damping contribution. The nonlinear behaviour of the aerodynamic loads can be also investigated, by changing the amplitude of the forced oscillation. Since one of the main objectives of the present work is the evaluation of the linear eigenvalue analysis
10   predictions, modal amplitude was kept low and equal to 0.2 m at the blade tip. As previously the analysis focuses on the yaw angle of 30° where stall induced vibrations mainly take place and only on rotor modes.

In the present analysis work computations have been performed using both ONERA and BL modeling. Since the linearized version of the BL model is not available in GAST_lin, the aeroelastic modes predicted by ONERA unsteady aerodynamics are employed in all work computations. Under the assumption that aeroelastic mode shapes are not
15   significantly affected by different dynamic stall models such a comparison is regarded meaningful and can address differences between the two models in predicted unsteady hysteresis loops and resulting work distributions along the span of the blades.

In Figure 25 & Figure 26 aerodynamic work results (integrated over the span and summed up for the three blades) are compared against eigenvalue analysis results both for steady-state and unsteady aerodynamics. The cross comparison of the
20   two sets can be only performed at a qualitative level because in order to obtain the nonlinear damping of a particular mode through work computations the predicted work value must be divided by the modal mass of the mode which is not the same for the different modes.

For steady-state aerodynamics (see Figure 25) the agreement between work computations and eigenvalue analysis results is very good. Some differences are only noted in the shape of the work distribution of M4. Eigenvalue analysis predicts
25   almost constant high positive damping of about 250% in the azimuth range [25°, 75°]. In the work results, despite the high work values obtained in the same azimuth range, a peak value is predicted at the azimuth angle of 50°. As in the eigenvalue analysis M8 remains positively damped at all azimuth angles while M3 exhibits negative damping values in the azimuth ranges [0°, 25°] and [75°, 120°]. Both methods agree that the damping of M7 is negative at all azimuth angles and that M5 and M6 are mostly positively damped.

30   For unsteady aerodynamics (see Figure 26) and in regard to flap modes, a good correlation between work results and eigenvalue analysis results predicted with ONERA model is obtained. Higher differences are noted in M3 but only at specific azimuth angles (for example 5° and 115°). In these particular azimuth positions the eigenvalue analysis predicts positive damping, while in work analysis damping is negative. When comparing work results of the two unsteady

aerodynamic models (ONERA vs. BL) again reasonable agreement is obtained. Higher differences are seen in M3 and M4 when the damping of the two modes drops. Overall BL model seems to predict higher minimum work of the above modes.

In regard to the edgewise modes, the results of the work analysis also compare well with the results of the eigenvalue analysis. The work calculated for mode M7 by ONERA model remains negative over the whole azimuth range whereas the same calculation for M5 and M6 gives positive work values. This is in line with the results of the eigenvalue analysis using the same dynamic stall model. When comparing work results of the two unsteady aerodynamic models (ONERA vs. BL) the highest differences are seen in M5. In the azimuth range of [0°,20°] and [80°,120°] ONERA model predicts lower work values that become negative in the azimuth range [95°,105°]. On the other hand, BL work predictions are shifted to slightly lower values for M6 and obtain negative values in the azimuth ranges [0°,15°] and [105°,120°]. In M7 both unsteady aerodynamic models agree that it is the lowest damped mode that obtains negative work values over the whole azimuth range.

It is noted that differences between eigenvalue analysis and work results in the shape of the curves are bigger in the case of unsteady aerodynamics. Despite the relatively small amplitude of 0.2 m used in the work analysis deviations from the eigenvalue analysis results are big in some cases. The explanation of the above differences lies in the strong nonlinearity of the ONERA equations, especially within the stall region. As described in sect. 3.2, in ONERA model, dynamic stall aerodynamic forces are derived through the solution of a set of first and second order in time, variable coefficient (coefficients depend on steady-state polars) differential equations. In regions where the gradient of the steady-state polars changes rapidly the linearized set of equations fails to represent correctly the actual nonlinear nature.

(a)   (b)
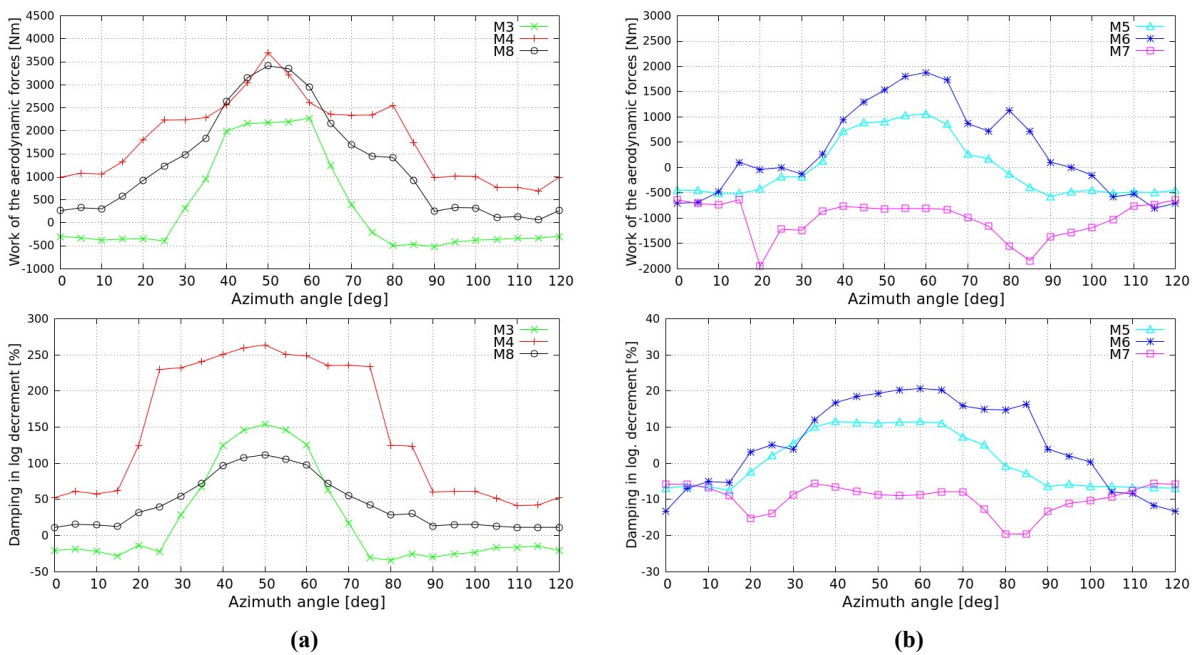
Figure 25.Comparison between aerodynamic work (0.2m modal amplitude) and damping results versus azimuth angle for steady-state aerodynamics; U=42.5 ms⁻¹ and yaw=30°. (a) in-plane (flapwise) modes, (b) out-of-plane (edgewise modes)
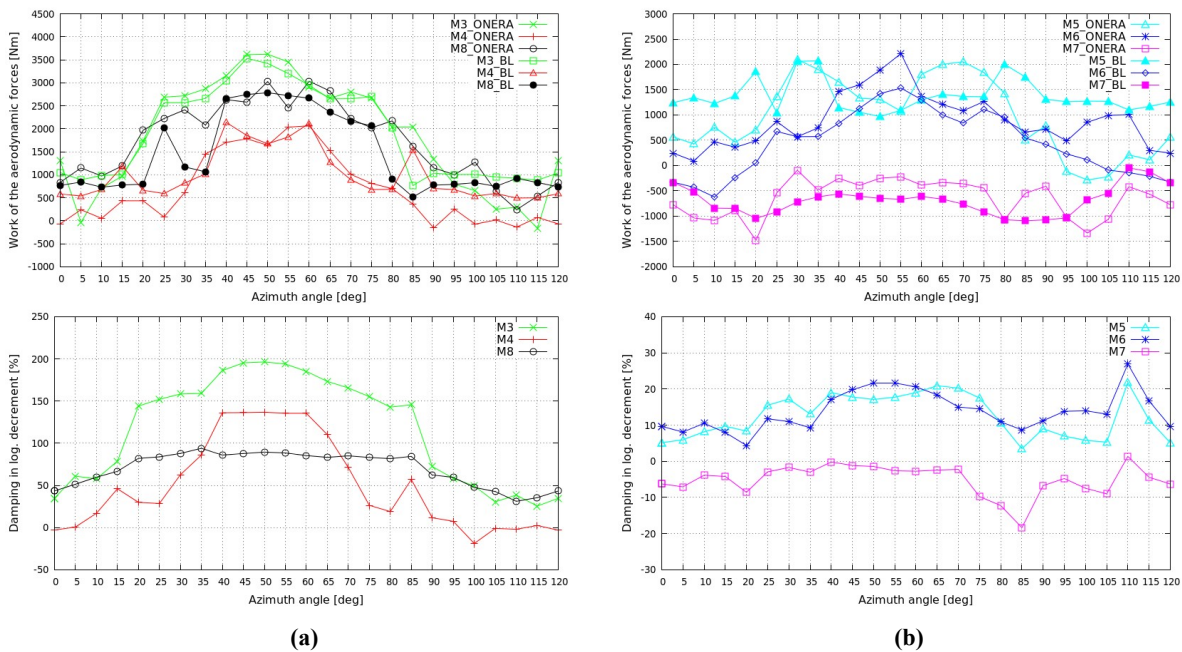
Figure 26. Comparison between aerodynamic work (0.2m modal amplitude) and damping results versus azimuth angle for unsteady aerodynamics (ONERA and BL model); U=42.5 ms⁻¹ and yaw=30°. (a) in-plane (flapwise) modes, (b) out-of-plane (edgewise modes)

In Figure 27 a snapshot of the shape of the negatively damped M7 mode is shown along with the traces of the three blades tip motion. Clearly, the mode is an asymmetric, out-of-plane one with the two lower blades moving in one direction while the upper in the opposite. Modal motion resembles tilting of the rotor and that is why the mode is called asymmetric out-of-plane tilt. It is seen that the three blades undergo a coupled edgewise/flapwise motion (elliptical shape of modal displacement loops) with a different degree of coupling (indicated by the slope of the loops) and different phase difference of the two motions (indicated by the width of the loops). All three blades follow an anti-clockwise rotation (indicated by the symbol in the loops which denotes the starting point on the loop). It is interesting to note that blade 3 essentially undergoes an in-plane motion (flapwise motion) while blade 1 presents the lowest degree of coupling with the flapwise direction.

In Figure 28 & Figure 29, work distributions along the three blades and C_L hysteresis loops (unsteady simulation results) of the three blades at r/R=0.90 are shown for M7 and for the azimuth angles of 20° and 100°. Simulations have been performed using both unsteady aerodynamic models (ONERA and BL). For the above azimuth angles the work calculations using the ONERA model predict highest negative work values of the particular mode. In the abovementioned plots 1 m amplitude of the blade tip motion has been considered. Wider hysteresis loops are attained in this way and thereby the unsteady character of the flow is better illustrated. At 20° rotor azimuth, both unsteady models agree that blade 2 (located at 140° azimuth) provides the highest negative work. As seen in the C_L-AOA plot blade 2 experiences AOA in the post stall region at negative angles. In agreement with the results for the pitching airfoils presented in Sect. 3.2 the ONERA model predicts wider dynamic stall loop for blade 2. Negative work is also contributed by blade 1 (located at 20°). Blade 1 operates

in the post stall region at positive AOA. Again, ONERA model predicts a wider loop than BL model. The difference in the shape of the C_L-AOA loops between blade 1 and blade 2 (both lying in the post stall region) is due to the different motions (in terms of flap-edge coupling and phase difference between the two directions of motion) undergone by the two blades in M7 (see Figure 27). Blade 1 motion is dominated by vibrations in the edgewise direction with low coupling with the flapwise direction (about 20%) while blade 2 exhibits a stronger flap-edge coupling. As a result of the lower flapwise component in blade 1 motion, the range of AOAs variation seen by blade 1 is low. The high width of blade 1 loop can be explained by the relatively high reduced frequency of the motion which is about $k = 0.14$ for this specific case (frequency 0.8 Hz, chord at 80 m span, 2.3 m, wind velocity 42.5 m/s). Comparing the work predictions of the two unsteady models they are found in a relatively good agreement. Some differences are noted in the mid span of blade 1 where ONERA model predicts higher work values. The airfoil sections of the mid span experience AOA in the vicinity of the C_{Lmax} angle and therefore the higher hysteresis predicted by ONERA model enhances the damping of the respective part of the blade. At 100° rotor azimuth, according to ONERA model, negative work is almost evenly contributed by blades 2 and 3 (located at 220° and 340° respectively). The shapes of the C_L-AOA loops of blade 1 on one hand, and of blades 2 and 3 on the other, are quite different. This is mainly because of the different flow conditions encountered by the different blades. Blades 2 and 3 operate in deep stall (well within the negative C_L-AOA slope region) while blade 1 encounters light stall conditions (mainly positive slopes up to the C_{Lmin}). BL model predicts considerably lower negative work values along the span of blade 2 as compared to ONERA model. As seen in the loops plot there is a distinct difference in the slopes of the loops provided by the two models. BL loop has clearly higher slope justifying the higher work values predicted by the model. On blade 1, BL model predictions agree with ONERA results that the loop obtains a positive slope however the width of the loop predicted by BL model is narrower. Similar loops and work distributions are predicted by both models on blade 3.
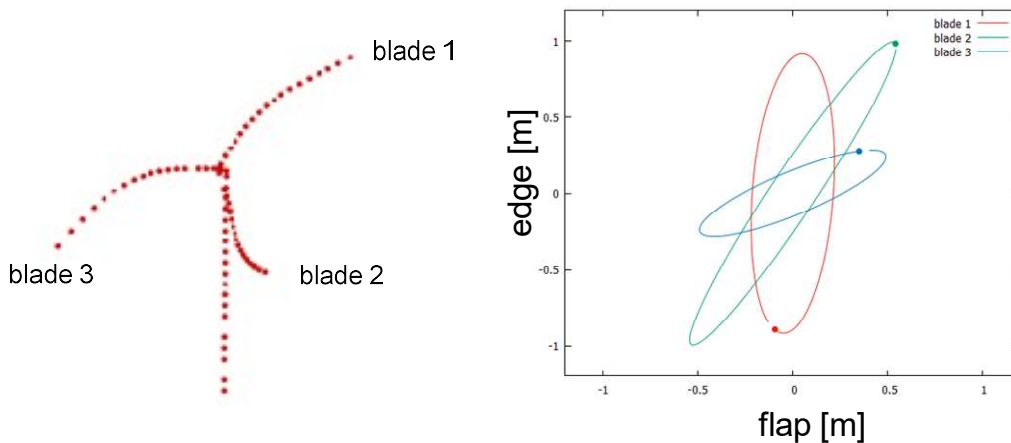
Figure 27. Shape of the lowest damped M7 mode at the azimuth angle of 20°. Trace of the modal displacement of the three blades.

It is also noted that the results of the work analysis seem to agree well with the results of the time domain simulations in turbulent inflow (depicted in Figure 13). In both sets, at the rotor azimuth of 20° the blade which has an azimuth angle of 20° is lying in the post stall region at positive AOA, the blade with azimuth angle 140° is facing stall at negative AOA and the blade with azimuth angle 260° is also experiencing negative AOA but in the attached flow region. Similarly, for the rotor azimuth of 100° the blade which is positioned at 100° angle, is experiencing negative AOA close to C_{Lmin} angle while the other two blades operate in deep stall at negative and positive AOA respectively.

(a)   **(b)**
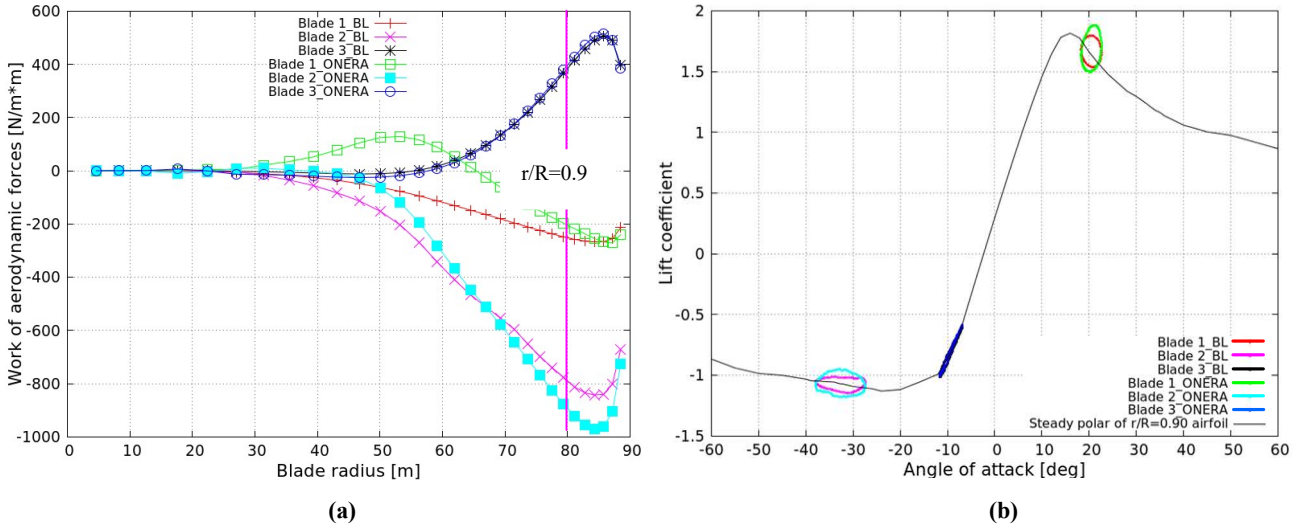
Figure 28.(a) Distribution of aerodynamic work over the three blades for mode M7. Azimuth angle 20°, (b) CL-AOA loops of the three blades at r/R=0.90 for mode M7. Azimuth angle 20°.

(a)   **(b)**
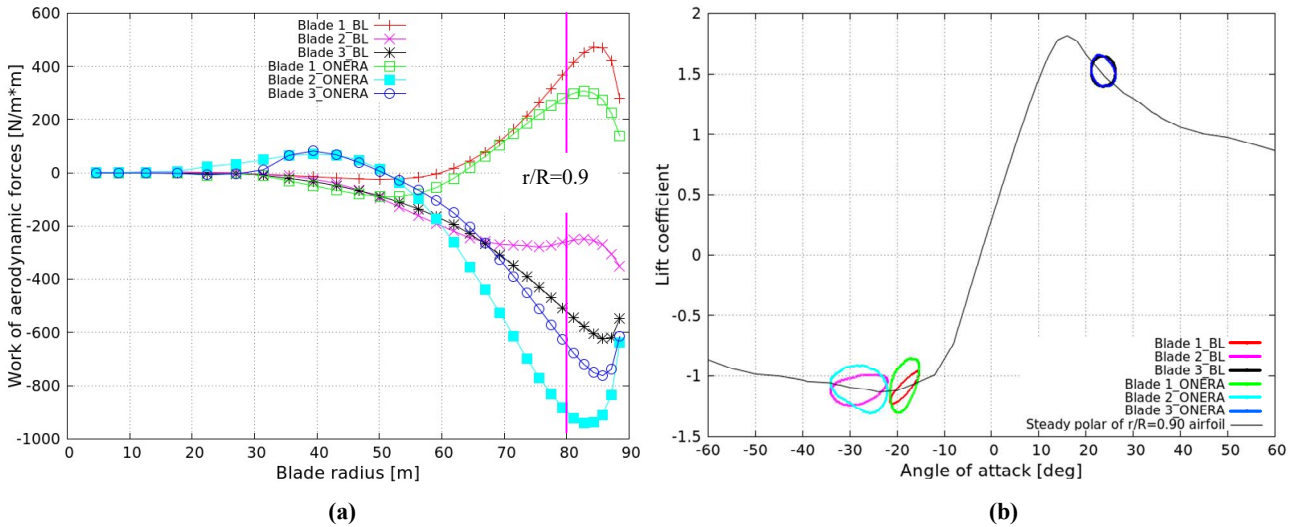
Figure 29.Distribution of aerodynamic work over the three blades for mode M7. Azimuth angle 100°, (b) CL-aoa loops of the three blades at r/R=0.90 for mode M7. Azimuth angle 100°.

5   Conclusions

The aeroelastic stability characteristics of the DTU 10 MW reference wind turbine in standstill or slowly idling operation have been numerically analysed. To this end, a consistent and computationally cost effective modeling environment has been presented. It is composed by the core eigenvalue stability analysis tool GAST_lin supported by the nonlinear time domain aeroelastic analysis code hGAST and a nonlinear stability analysis tool in which damping is assessed through computations of the aerodynamic work under imposed periodic motion. The predictions of the eigenvalue tool are evaluated through comparisons with the results of both nonlinear tools. It is a model based validation of the linearized model against its nonlinear counterparts. The cross-comparison of the above tools proved that fast linear eigenvalue stability tools can be used as a basis for characterizing stability of turbines in idling operation.

It is noted that the proposed eigenvalue stability analysis cannot always give a definite answer to the question whether the system has adequate damping or not. An example to that, is when a mode is positively damped in one part of the revolution and negatively damped in another. However, this definite answer is also difficult to be given even by Floquet analysis (or any other type of analysis). This is first because of the strong nonlinearity of the aerodynamics in dynamic stall but most importantly because of the effect that turbulent wind has on the behavior of the system. It is noted that turbulent wind cannot be easily accounted for in any stability analyses. An example of such an uncertainty is already given in the paper. Under uniform inflow conditions (wind speed 42.5ms^{-1} and yaw 30°) the system is unstable, as shown in Figure 22. Vibrations continuously grow in time and lead to divergence after a certain time. This is in agreement with the eigenvalue analysis results which predict that M7 remains negatively damped throughout the revolution. Also, the frequency of the predicted negatively damped mode M7 agrees with the PSD of the edgewise moment which exhibits a peak at the frequency of 0.8 Hz. For the same case and for turbulent inflow conditions, vibrations do no lead to critical instabilities of the system. Amplifying edgewise vibrations are observed in part of the time series of Figure 13 which after certain time decay. This is because, as a result of the turbulent wind, operation moves continuously in and out the negative C_L slope region as indicated in the C_L-AoA loops of Figure 14. So, the eigenvalue tool should not be considered as a standalone tool for assessing stability behavior of the idling turbine. It should be used in combination with nonlinear tools. The aim of the proposed computational environment is to identify conditions that favor instabilities which could be the starting point for improving blade structural dynamics or/and aerodynamics.

The analysis showed that the lowest damped modes of the 10 MW idling rotor are the out-of-plane ones (symmetric and asymmetric). At yaw misalignment of 30° the asymmetric out-of-plane tilt mode attains negative damping throughout the entire range of azimuth angles. At higher yaw angles stability of the rotor is gradually restored and the damping of the out-of-plane modes returns to positive values. At the yaw angle 30° maximum edgewise loads of the time domain analysis are also obtained. At the above conditions, instabilities are noted in the results of the time domain analysis which through FFT on loads are identified to be linked to the negatively damped out-of-plane tilt mode. Although the instabilities seen in the results of the time domain analysis are not continuously growing as suggested by the negative damping of the eigenvalue

predictions they lead to some quite severe stall induced vibrations in the edgewise direction. The less coherent loading conditions developing over the rotor disk under turbulent inflow lead to mitigated vibrations as compared to the uniform inflow case considered in the stability analysis. As a result of the temporal and spatial variation of the wind the blades are continuously pushed in and out of the negative C_L slope regions and therefore vibrations do not have enough time to build up. At higher yaw angles edgewise loads decrease in agreement with the results of the eigenvalue analysis which predicts positive damping values of the out-of-plane modes at yaw angles higher than 30°.

Eigenvalues stability analyses are performed both for steady-state and unsteady aerodynamics. The aim of running simulations also for steady state aerodynamic conditions is to explore the range of damping predictions especially in connection to the fact that many of the state of the art engineering dynamic stall models automatically switch to steady state at very high AOA. Results indicate that steady state analysis is more conservative providing higher negative damping values for all out-of-plane modes. Overall the agreement of the eigenvalue stability analysis with the work computations is good. Some higher differences are noted at specific azimuth positions when unsteady aerodynamics is employed. The differences are mainly due to the strong nonlinearity of the ONERA equations and triggered especially in deep stall conditions.

6   Acknowledgments

The work presented in paper was partially funded from the European Community's Seventh Framework Program under grant agreement No. FP7-ENERGY-2012-1-2STAGE-308974 (INNWIND.EU) and No. FP7-ENERGY-2013-1/no.608396 (AVATAR).

References

Bak, C., Fuglsang, P., Johansen, J, Antoniou, I.: Wind Tunnel Tests of the NACA 63-415 and a Modified NACA 63-415 Airfoil, Risø-R-1193(EN), Risø National Laboratory, Roskilde, Denmark, December 2000

Bak, C., Zahle, F., Bitsche, R., Kim, T., Yde, A., Henriksen, L.C., Natarajan, A., Hansen, M.H.,: Description of the DTU 10MW Reference Wind Turbine, DTU Wind Energy Report-I-0092, 2013.

Bottasso, C., Cacciola, S.: Model independent periodic stability analysis of wind turbines, Wind Energy, 2015, 18(5), pp 865-887

Coleman, R.P., Feingold, A.M.: Theory of self excited mechanical oscillations of helicopter rotors with hinged blades, Technical Report NACA–TN-3844, NACA-TR-1351, Langley Research Center, 1958.

Fuglsang, P., Antoniou, I., Dahl, K.S., Madsen, H.A.: Wind Tunnel Tests of the FFA-W3-241, FFA-W3-301 and NACA 63430 airfoils, Risø-R-1041(EN), Risø National Laboratory, Roskilde, Denmark, December 1998

Hansen, M. H.: Improved Modal Dynamics of Wind Turbines to Avoid Stall-Induced Vibrations, Wind Energy, 2003, 6, 179–195.

Hansen, M.H., Gaunaa, M., Madsen, H.A.:A Beddoes-Leishman type dynamic stall model in state-space and indicial formulation,Risoe Report, Risoe-R-1354(EN), 2004.

Hansen, M. H.: Aeroelastic instability problems for wind turbines, Wind Energy, 2007, 10, 551–577.

Heinz, J.C., Sørensen, N.N., Zahle, F., Skrzypiński, W.: Vortex-induced vibrations on a modern wind turbine blade, Wind Energy, 2016, DOI: 10.1002/we.1967

Manolas D.I., Riziotis, V.A., Voutsinas, S.G: Assessing the importance of geometric nonlinear effects in the prediction of wind turbine blade loads, Computational and Nonlinear Dynamics Journal, Vol. 10, 041008, July 2015.

Petersen, J.T., Madsen, H.A., Bjorck, A., Enevoldsen, P., Øye, S., Ganander, H. and Winkelaar, D.: Prediction of Dynamic Loads and Induced Vibrations in Stall, Risø–R–1045(EN), Risø National Laboratory, Roskilde, 1998.

Petot, D.: Differential Equation Modeling of Dynamic Stall, Recherché Aerospatiale, 1989, 5, 59–72.

Politis, E.S., Chaviaropoulos, P.K., Riziotis, V.A., Voutsinas, S.G., Romero-Sanz, I.: Stability analysis of parked wind turbine blades, Proceedings of the EWEC 2009, Scientific Track, Marseille, France, March 16-19.

Riziotis, V.A.: Aeroelastic analysis of stall on wind turbine rotors, PhD thesis, 2003

Riziotis, V.A., Voutsinas, S.G., Politis, E.S., Chaviaropoulos, P.K.: Aeroelastic stability of wind turbines: the problem the methods and the issue, Wind Energy, 2004, 7, pp 373-392.

Shi, L., Riziotis, V.A., Voutsinas, S.G, Wang, J.: A consistent vortex model for the aerodynamic analysis of vertical axis wind turbines, Journal Wind Engineering and Industrial Aerodynamics 135 (2014) 57-69.

Skrzypiński, W., Gaunaa, M., Sørensen, N., Zahle, F., Heinz, J.: Self-induced vibrations of a DU96-W-180 airfoil in stall, Wind Energy, 2014a, 17 (4), pp 641–655,

Skrzypiński, W., Gaunaa, M., Sørensen, N., Zahle, F., Heinz, J.: Vortex-induced vibrations of a DU96-W-180 airfoil at 90° angle of attack, Wind Energy, 2014b, 17 (10), pp. 1495-1514

Skrzypiński, W., Gaunaa, M.: Wind turbine blade vibration at standstill conditions — the effect of imposing lag on the aerodynamic response of an elastically mounted airfoil, Wind Energy, 2015, 18(3), pp 515–527

Skrzypiński, W., Gaunaa, M., Heinz, J.: Modeling of vortex-induced loading on a single blade installation-setup, The Science of Making Torque from Wind Conference, TORQUE 2016, Munich, Germany, 5-7 October, Journal of Physics: Conference series 753 (2016) 082037.

Skjoldan, P.F., Hansen, M.H.,:On the similarity of the Coleman and Lyapunov - Floquet transformations for modal analysis of bladed rotor structures, Journal of Sound and Vibration, 327, 2009, pp.424–439.

Wang, K., Riziotis, V.A., Voutsinas, S.G.: Aeroelastic Stability of Idling Wind Turbines, Proceedings of the Science of Making Torque from Wind Conference, TORQUE 2016, Munich, Germany, 5-7 October.

Zou, F., Riziotis, V.A., Voutsinas, S.G, Wang, J.:Analysis of vortex and stall induced vibrations at standstill conditions using a free wake aerodynamic code,Wind Energy, 2015, 18(12), pp 2145-2169.